A Change Detector Based on an Optimization with Polarimetric SAR imagery

Armando Marino, *Member, IEEE*, Irena Hajnsek, *Member, IEEE*

Abstract

The possibility to detect changes in land cover with remote sensing is particularly valuable considering the current availability of long time series of data. SAR can play an important role in this context, since it can acquire complete time series without limitations of cloud cover. Additionally, polarimetry has the potential to improve significantly the detection capability allowing the discrimination between different polarimetric targets. This paper is focused on developing two new methodologies for testing the stability of observed targets (i.e. Equi-Scattering Mechanisms hypothesis) and change detection. Both the algorithms adopt a Lagrange optimization, which can be performed with two eigen-problems. Interestingly, the two optimizations share the same eigenvectors. Three statistical tests are proposed to set the threshold for the change detector. Two of them are mostly aimed at point targets and one is more suited for distributed targets.

All the algorithms and procedures developed in this paper are tested on two different quad-polarimetric dataset acquired by the E-SAR DLR system in L-band (SARTOM 2006 and AGRISAR 2006 campaigns). The dataset are accompanied by ground surveys. The detectors are able to identify targets and areas with validated changes or showing clear differences in the images. The theoretical pdf exploited to model the optimum ratio fits adequately the data and therefore has been used for the statistical tests. Regarding the output of the tests, two of them provided good results, while one needs more care and adjustments.

Armando Marino and Irena Hajnsek are with ETH Zurich, Institute of Environmental Engineering, Zurich, Switzerland (e-mail: marino@ifu.baug.ethz.ch). Irena Hajnsek is also with the German Aerospace Center (DLR), High Frequency Department, Wessling, Germany.

© 2013 IEEE. Personal use of this material is permitted. Permission from IEEE must be obtained for all other uses, in any current or future media, including reprinting/republishing this material for advertising or promotional purposes, creating new collective works, for resale or redistribution to servers or lists, or reuse of any copyrighted component of this work in other works.

Keywords

Synthetic Aperture Radar, Polarimetry, Change Detection, Equi-Scattering Mechanisms.

I. INTRODUCTION

Change detection is a valuable topic in SAR remote sensing and polarimetry can improve the results of single polarimetric algorithms [1], [2], [3], [4], [5], [6]. The polarization of the transmitted and received waves can be exploited to extract more information about the observed targets, since different targets are expected to have different polarimetric behaviors. Besides the physical rationale, polarimetry allows to acquire four images that will naturally bring more information compared to a single image (unless the three images are perfectly correlated, which is generally not the case). From a mere signal processing point of view, this information is supposed to improve the detection output.

The aim of this paper is to develop an algorithm aimed at change detection and evaluate the error made after the Equi-Scattering Mechanism (ESM) hypothesis [7], [8], [9]. A very brief introduction to polarimetry will be provided here with the mere purpose to show the tools exploited in the following.

A single target is defined as a deterministic target which does not change its polarimetric behavior in time/space. Therefore, it can be represented by a single scattering matrix $[S]$ or equivalently a single scattering vector [7], [10]:

$$\underline{k}_L = [HH, HV, VH, VV]^T, \tag{1}$$

where H and V stands for linear horizontal and vertical and the repeated letter is for transmitter-receiver. The previous is obtained employing the Lexicographic basis set. In the case of a reciprocal medium and monostatic sensor, $HV = VH$ and $\underline{k}_L$ is three-dimensional complex

(i.e. $\underline{k}_L \in \mathbb{C}^3$) [7]. Another largely used basis set to convert $[S]$ into a scattering vector is the Pauli basis. In the reciprocal case, this is $\underline{k}_P = 1/\sqrt{(2)}\,[HH + VV, HH - VV, 2 * HV]^T$. A Scattering Mechanisms (SM) $\underline{\omega}$ is an ideal target and is defined as a normalized scattering vector: $\underline{\omega} = \frac{\underline{k}}{|\underline{k}|}$.

The targets observed by a SAR system are often distributed over an area larger than the resolution cell and composed by different objects. For this reason, each pixel of such distributed targets has a specific polarimetric behavior. Such targets take names of *partial targets* and they can be characterized via their second order statistics [7], [10]. In this context, a target covariance matrix can be estimated as $[C] = \langle \underline{k}\ \underline{k}^{*T} \rangle$, where $\langle . \rangle$ is the finite averaging operator. In case that the Single Look Complex (SLC) pixel can be modeled by a Complex Gaussian, the second order statistics are necessary and sufficient to completely characterize a partial target. In case of the Pauli basis, the covariance matrix is indicated by $[T]$ and takes the name of *Coherency* matrix.

If two different acquisitions $\underline{k}_1$ and $\underline{k}_2$ are available two SM $\underline{\omega}_1$ and $\underline{\omega}_2$ can be considered and a polarimetric and interferometric coherence can be estimated [8], [9]:

$$\gamma = \frac{\underline{\omega}_1^{*T}[\Omega_{12}]\underline{\omega}_2}{\sqrt{(\underline{\omega}_1^{*T}[T_{11}]\underline{\omega}_1)\ (\underline{\omega}_2^{*T}[T_{22}]\underline{\omega}_2)}}, \tag{2}$$

where $[T_{11}] = \langle \underline{k}_1\ \underline{k}_1^{*T} \rangle$, $[T_{22}] = \langle \underline{k}_2\ \underline{k}_2^{*T} \rangle$ and $[\Omega_{12}] = \langle \underline{k}_1\ \underline{k}_2^{*T} \rangle$.

In the following the hypothesis of Equi-Scattering Mechanisms (ESM) is tested [7], [11]. The latter assumes that the partial target under analysis does not change during the two acquisitions. It is generally followed by two positions:

1. γ is estimated on two identical $\underline{\omega}$: i.e. $\underline{\omega}_1 = \underline{\omega}_2$. This avoids decorrelation effects due to the change of selected target.

2. The second order statistics of the partial targets in the first and second acquisitions are the

same: i.e. $E\left[\underline{k}_1\,\underline{k}_1^{*T}\right] = E\left[\underline{k}_2\,\underline{k}_2^{*T}\right]$.

The second hypothesis is operatively applied considering finite averaging, leading to $[T_{11}] = [T_{22}]$. Furthermore, it is defined the matrix $[T] = ([T_{11}] + [T_{22}])/2$ and the corresponding interferometric coherence can be written as:

$$\gamma_{ESM} = \frac{\underline{\omega}^{*T}[\Omega_{12}]\underline{\omega}}{\underline{\omega}^{*T}[T]\underline{\omega}}. \tag{3}$$

From a mathematical point of view the expression of γ_{ESM} is easier to tackle than γ. This led to the proliferation of algorithms working on γ_{ESM} more than γ [7], [12], [13].

II. Optimizations

A. Error factor for Equi-Scattering Mechanisms (ESM)

The ESM hypothesis assumes that the partial target does not change polarimetrically between the two acquisitions. This of course is not always the case and some test has to be devised able to tell when the hypothesis is fulfilled or when it will introduce errors in the estimations. A test for ESM based on *Geometrical Perturbation* filters [14], [15] was already developed by the authors [16]. The main characteristic of such test is the capability to separate polarimetric information from the overall power of the partial target (i.e. Trace of the covariance matrix). It is valuable for testing the feasibility of a ESM hypothesis because the Pol-InSAR coherence γ is independent of changes in the Trace of the matrices.

In this paper, a different approach is followed which will lead to a complementary results to the one obtained in [16]. After $\underline{\omega} = \underline{\omega}_1 = \underline{\omega}_2$ is considered, the Pol-InSAR coherence can always be written as:

$$\gamma = \frac{\underline{\omega}^{*T}[\Omega_{12}]\underline{\omega}}{\underline{\omega}^{*T}[T]\underline{\omega}} \frac{\underline{\omega}^{*T}[T]\underline{\omega}}{\sqrt{(\underline{\omega}^{*T}[T_{11}]\underline{\omega})\ (\underline{\omega}^{*T}[T_{22}]\underline{\omega})}} = \gamma_{ESM}\gamma_e. \tag{4}$$

To make the formulation more compact, the quadratic forms in the denominator can be identified as $P_1 = \underline{\omega}^{*T}[T_{11}]\underline{\omega}$ and $P_2 = \underline{\omega}^{*T}[T_{22}]\underline{\omega}$. Few properties of the factor γ_e are:

1. It is real positive (i.e. $\gamma_e \in \mathbb{R}^+$) since all its composing elements belong to $\mathbb{R}^+$.
2. It is defined in the interval $\gamma_e \in [1, \infty[$:

$$\gamma_e = \frac{(P_1 + P_2)/2}{\sqrt{P_1 * P_2}} = \frac{AM}{GM} \geq 1, \tag{5}$$

where AM stands for Arithmetic Main and GM for Geometrical Main and it is always $AM \geq GM \;\; \forall P_1, P_2 \in \mathbb{R}^+$.

3. $\gamma \geq \gamma_{ESM} \;\; \forall [T_{11}], [T_{22}], [\Omega_{12}]$. This comes from the previous property.

The main idea of the proposed methodology is to retrieve the stationary points of γ_e in order to understand which are the SM that suffer more (less) from the ESM assumption. This also returns the maximum error made after the ESM hypothesis is adopted. The optimization can be easily accomplished with a Lagrange methodology, where the numerator is optimized while the denominator is constrained to be constant [17]. Please note, this is a methodology largely exploited in the SAR polarimetric community [7], [10].

To be more general, the derivation will be made considering $\underline{\omega}_1 \neq \underline{\omega}_2$. The Lagrangian is:

$$L = \underline{\omega}_1^{*T}[T]\underline{\omega}_2 - \lambda_1 \left(\underline{\omega}_1^{*T}[T_{11}]\underline{\omega}_1 - C_1\right) - \lambda_2 \left(\underline{\omega}_2^{*T}[T_{22}]\underline{\omega}_2 - C_2\right). \tag{6}$$

$$\begin{aligned} \frac{\partial L}{\partial \underline{\omega}_1^{*T}} &= [T]\underline{\omega}_2 - \lambda_1[T_{11}]\underline{\omega}_1 = 0 \\ \frac{\partial L}{\partial \underline{\omega}_2^{*T}} &= [T]^{*T}\underline{\omega}_1 - \lambda_2[T_{22}]\underline{\omega}_2 = 0 \end{aligned} \tag{7}$$

After few calculations the system of equations can be found, which corresponds to two di-

agonalizations:

$$[T_{11}]^{-1}[T][T_{22}]^{-1}[T]\underline{\omega}_1 = \lambda_1\lambda_2^{*T}\underline{\omega}_1, \tag{8}$$

$$[T_{22}]^{-1}[T][T_{11}]^{-1}[T]\underline{\omega}_2 = \lambda_2\lambda_1^{*T}\underline{\omega}_2.$$

After some algebraic manipulations, it is possible to derive the identity:

$$[T_{11}]^{-1}[T][T_{22}]^{-1}[T] = [T_{22}]^{-1}[T][T_{11}]^{-1}[T] = \frac{1}{4}\left[[T_{22}]^{-1}[T_{11}] + 2[I] + [T_{11}]^{-1}[T_{22}]\right] = [A]. \tag{9}$$

Therefore, only one diagonalization has to be performed:

$$\underset{\underline{\omega}\in\mathbb{C}^3}{Opt}\gamma_e \rightarrow [A]\underline{\omega} = \lambda_e\underline{\omega}. \tag{10}$$

After the diagonalization it will be possible to express $[A]$ with eigenvectors and eigenvalues: $[A] = [U_e]^{*T}[\Sigma_e][U_e]$, where $[\Sigma_e] = diag(\lambda_{1e}, \lambda_{2e}, \lambda_{3e})$ with $\lambda_{1e}, \lambda_{2e}, \lambda_{3e} \in \mathbb{R}^+$ and the columns of $[U_e]$ are the eigenvectors. The eigenvalues correspond to the maximum or minimum errors committed in the estimation of the PolInSAR coherence after the ESM assumption and the eigenvectors represent the scattering mechanisms suffering such errors.

Since the matrix $[A]$ is generally not Hermitian the eigenvectors are not expected to be orthogonal (i.e. the maximum and minima of γ_e are generally not constrained to be orthogonal each other). In the next section, a proof will be provided that the eigenvalues of $[A]$ exist and are always real positive for all T_{11} and T_{22} Hermitian semi-positive definite matrices.

B. Change detection with power ratio

The previous algorithm is not directly focused on change detection. The aim of this section is to understand if a similar methodology can be exploited to optimize another polarimetric observable (i.e. operator) that has more relevance for change detection. The ratio of the

power in the two acquisitions varying the SM is selected:

$$\underset{\underline{\omega}\in\mathbb{C}^3}{Opt}\,\rho_{12},\quad \rho_{12}=\frac{\underline{\omega}^{*T}[T_{11}]\underline{\omega}}{\underline{\omega}^{*T}[T_{22}]\underline{\omega}}. \tag{11}$$

Mathematically, this is the ratio of two quadratic forms that are real positive, since the matrices $[T_{11}]$ and $[T_{22}]$ are Hermitian semi-positive definite. The optimization can be again accomplished with a Lagrangian methodology which ends in a diagonalization:

$$\begin{aligned} L&=\underline{\omega}^{*T}[T_{11}]\underline{\omega}-\lambda(\underline{\omega}^{*T}[T_{22}]\underline{\omega}-C), \\ \frac{\partial L}{\partial \underline{\omega}^{*T}}&=[T_{11}]\underline{\omega}-\lambda[T_{22}]\underline{\omega}=0 \\ [T_{22}]^{-1}[T_{11}]\underline{\omega}&=\lambda\underline{\omega}. \end{aligned} \tag{12}$$

To conclude, $[T_{22}]^{-1}[T_{11}]=[U_r]^{*T}[\Sigma_r][U_r]$, where $[\Sigma_r]=diag(\lambda_{1r},\lambda_{2r},\lambda_{3r})$ with $\lambda_{1r},\lambda_{2r},\lambda_{3r}\in\mathbb{R}^+$ and the columns of $[U_r]$ are the eigenvectors. The maximum eigenvalue λ_{1r} represents the maximum ratio ρ_{12}. In order to understand if this is the $\underline{\omega}$ suffering the maximum change in the two acquisitions, another optimization should be performed. This is the ratio:

$$\rho_{21}=\frac{\underline{\omega}^{*T}[T_{22}]\underline{\omega}}{\underline{\omega}^{*T}[T_{11}]\underline{\omega}}, \tag{13}$$

which ends up with the diagonalization of the matrix: $[T_{11}]^{-1}[T_{22}]$. This is because the power could increase or decrease in the two acquisitions (i.e. the target could appear either in the first or second acquisitions). Therefore, the scattering mechanism that suffers the maximum change $\underline{\omega}_{max}$ is:

$$\underline{\omega}_{max}=Argmax\left[\underset{\underline{\omega}\in\mathbb{C}^3}{Opt}\,\rho_{12},\underset{\underline{\omega}\in\mathbb{C}^3}{Opt}\,\rho_{21}\right]. \tag{14}$$

It is interesting to note that $([T_{11}]^{-1}[T_{22}])^{-1}=[T_{22}]^{-1}[T_{11}]$, therefore they will have the same eigenvectors, but inverted eigenvalues (the power of a matrix does not change the eigenvectors) [18]. Summarizing, diagonalizing $[T_{22}]^{-1}[T_{11}]$, all the information about the eigenvec-

tors and eigenvalues of its inverse will be available, and only one of the two problems has to be solved. This means that:

$$\underline{\omega}_{max} = Argmax \left[\underset{\underline{\omega} \in \mathbb{C}^3}{max}(\rho_{12}), 1/\underset{\underline{\omega} \in \mathbb{C}^3}{min}(\rho_{12}) \right]. \tag{15}$$

With the goal of improving the visualization of the results, the eigenvalues can be inverted when they are smaller than one and their sign changed (i.e. making it negative). In other words:

$$\begin{cases} \hat{\rho}_{max} = \rho_{max} & \text{if } \rho_{max} \geq 1, \\ \hat{\rho}_{max} = -\frac{1}{\rho_{max}} & \text{if } \rho_{max} < 1. \end{cases} \tag{16}$$

As a final remark, the optimization of the power ratio is a relatively old problem and a similar result was found by Novak et al. [19] and called Polarimetric Match Filter (PMF). In the PMF, the ratio is calculated between the power of the target and the surrounding clutter (generally estimated locally with guard windows). The optimization maximizes the contrast between target and clutter selecting the best SM to be used for the following detection (generally accomplished with a Constant False Alarm Rate methodology). Therefore, the PMF is applied over one quad-pol acquisition and exploited for target detection, while the change detector proposed here, exploits two quad-pol acquisitions.

C. Relationship between the two algorithms and discussion

In the previous sections two different optimizations were proposed, both based on diagonalizations of two defined matrices. It is interesting to understand if there is some relationship between the two set of solutions. In other words, are the $\underline{\omega}$ that change more also the one that suffer more after a ESM hypothesis (*ii*)? In Appendix, a proof is provided that the eigenvectors of γ_e are the same as the eigenvectors of ρ_{12}. Therefore, $[U_e] = [U_r][P],\ \forall [P]$

permutation matrix (i.e. the order of the columns of the eigenvectors matrix can be rearranged).

The proposed algorithms are sensitive to changes in the backscattering between the two images. This means that radiometric calibration errors between the two polarimetric acquisitions (i.e. the scattering matrix of the second acquisitions has a different gain than the one of the first acquisition) will be reveled by the detector. Therefore, this feature may have the potential to be exploited for performing some corrections in case of eventual calibration problems. It should also be noticed that if very small changes (ratio close to 1) of the backscattering over large areas is investigate, then special care should be taken in calibrating with high accuracy the data. Future work will be carried out on trying to exploit the proposed optimization to devise some procedure to improve the calibration.

Few words should be spent regarding the results of the ESM test. As mentioned previously, the authors already developed a ESM test based on Geometrical Perturbation filters [16]. The latter is particularly suited as a pre-processing test of the Pol-InSAR coherence γ, since this is independent of the total power of the partial target (i.e. Trace of the covariance matrix). However, after the ESM hypothesis is performed and we are interested in understanding the amount of error made, the analysis should be done on the ESM coherence γ_{ESM} more than the original Pol-InSAR coherence γ. γ_{ESM} is dependent on the overall amplitude of the partial target. In other words, if $\underline{k}_1 = c\underline{k}_2$ with $c \in \mathbb{R}$ the final value of γ_{ESM} would be different varying the factor c (i.e. $\lim_{c\to\infty}\gamma_{ESM} = 0$, while $\lim_{c\to\infty}\gamma = \gamma$).

To conclude, if the interest is to test whether the ESM hypothesis can be made or not (i.e. to produce a mask where the ESM assumption is fulfilled and where not) the algorithm based on Geometrical Perturbation should be employed [16]. On the other hand, if the ESM hypothesis cannot be avoided, because there is no other ways to solve the problem, than the

algorithm proposed here (based on the Lagrange optimization) should be exploited, since it provides a direct measure of the error made.

III. Statistical test

The aim of this section is to devise statistical tests aimed at setting the threshold of the proposed detectors. The first step is to know (or estimate) the *probability density function* (pdf) of the observable under analysis [20]. In this paper two optimizations were proposed: of γ_e and ρ_{12}. Unfortunately, the analytical expression of the pdf for γ_e is unknown and its evaluation is not trivial. On the other hand, the power ratio has a well-known distribution [10]. For this reasons, this paper is concentrated in developing statistical tests on the optimization of ρ_{12}. Finding the analytical version of the pdf of γ_e or fitting some known distribution will be subject of future analysis.

A. pdf of Power Ratio

An expression for the pdf of the powers (or intensities) ratio was already derived by Lee et al. [10]. This is based on the assumption that the initial complex pixel (SLC) can be modeled by a complex Gaussian process (i.e. texture effects are neglected) [21]. The expression for the Intensity Ratio (IR) pdf is:

$$f_R^{(n)}(r) = \frac{\tau^n \Gamma(2n)\left(1-|\rho|^2\right)^n (\tau+r) r^{n-1}}{\Gamma(n)\Gamma(n)\left[(\tau+r)^2 - 4\tau|\rho|^2 r^2\right]^{(2n-1)/2}}, \tag{17}$$

where n is the number of independent looks and Γ is the Gamma function. It has to be noted that such pdf is based on the knowledge of the true values of τ and ρ, which are defined by the underlying statistical distribution. If S_1 and S_2 are the two images composing the ratio,

the value of ρ can be estimated as:

$$\rho = \frac{\sum_{k=1}^{n} S_1 S_2^*}{\sqrt{\sum_{k=1}^{n} |S_1|^2 \sum_{k=1}^{n} |S_2|^2}} \tag{18}$$

and τ is estimated with:

$$\tau = \frac{\sum_{k=1}^{n} |S_1|^2}{\sum_{k=1}^{n} |S_1|^2}, \tag{19}$$

which are also the Maximum Likelihood Estimators (MLE) in case of Gaussian pixel. Clearly, exploiting the MLE estimates instead than the true values (which are unknown) may introduce some estimation error.

Figure 1 presents some plots varying different pdf parameters. In all the cases, the mean value of the ratio is $\tau = 5$. In the first two tests, the number of independent averaged pixels is varied keeping constant the correlation between the two images. As expected, increasing the number of looks the variance reduces while the mean does not change. In particular, if only one look is available the distribution resembles a negative exponential (as the distribution of a single look intensity). In the second test, the correlation between the two images is varied while the number of looks is kept constant. Interestingly, it appears that the more the images are correlated, the more the variance of the distribution reduces (even with one single look). In particular, given $\rho = 1$, the distribution is a Delta of Dirac centered on the mean value. In other words, if the two images are perfectly correlated each other, the detection becomes a deterministic problem and the speckle on the single images does not affect anymore the estimation of the ratio (i.e. the speckle cancels out in the ratio). This has large consequences when developing an anomaly detector as showed in the following.

A final remark is that the IR pdf was derived for the ratio of quadratic forms of the same matrix where $\underline{\omega}_1$ and $\underline{\omega}_2$ are kept constant. Having two different coherency matrices at the numerator and denominator is not problematic, since it can just be justified with a change of

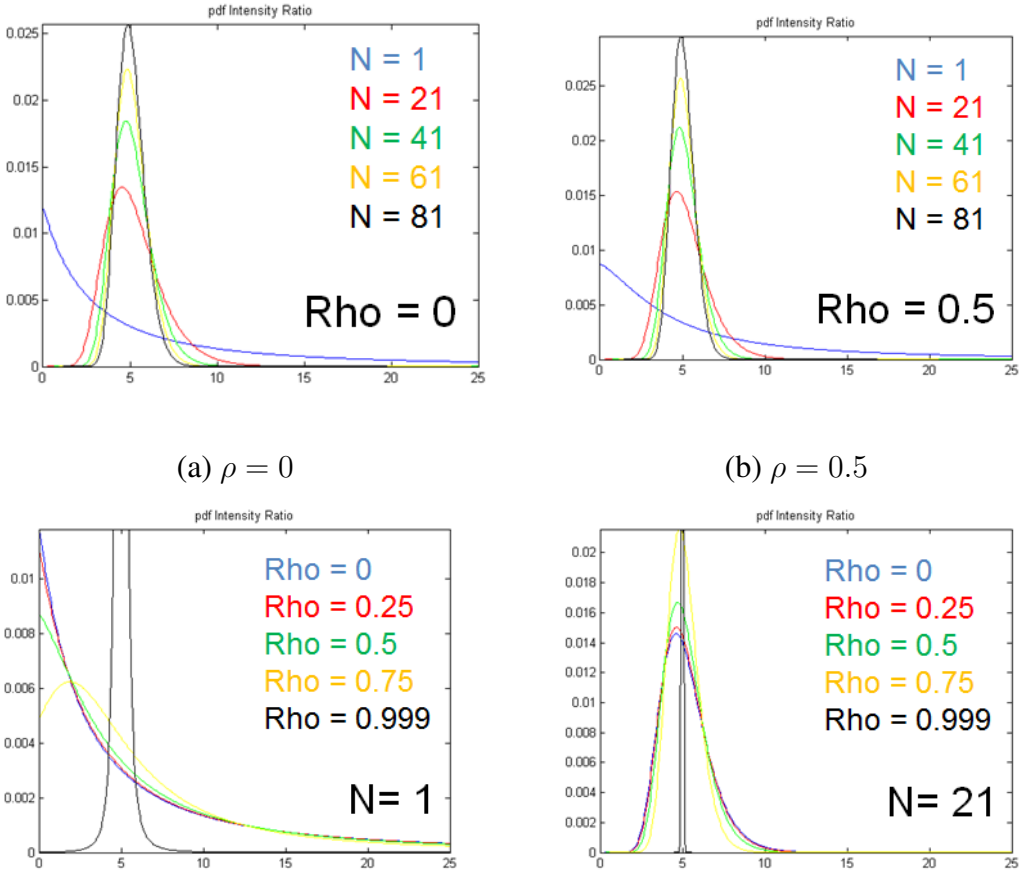

(a) $\rho = 0$ (b) $\rho = 0.5$

(c) $N = 1$ (d) $N = 21$

Fig. 1. pdf of Intensity/Power Ratio: (a) varying N and keeping $\rho = 0$; (b) varying N and keeping $\rho = 0.5$; (c) varying ρ and keeping $N = 1$; (d) varying and ρ keeping $N = 21$. The average value is $\tau = 5$ for all the plots.

the scattering mechanism and does not modify their statistics. In the case of the proposed detector, the ω is the result of an optimization and therefore can theoretically modify the target observed and therefore the distribution. Nevertheless, the IR pdf is a good approximation for homogeneous areas, since the partial targets in the two images are the same and therefore the $\underline{\omega}_{max}$ will not change (unless for some speckle effects that are reduced performing adequate averaging). On the other hand, if the scene presents some heterogeneity the IR is not satisfactory anymore. In actual fact, if the area is heterogeneous the IR pdf will not work even in the case of the classic polarimetric ratio, since it assumes homogeneous Gaussian scattering. In the validation section the fit will be analyzed in order to assess the feasibility of the IR pdf for the optimized ratio. Besides, in the future more work will be focused on trying to include some texture parameter in the pdf of the intensity ratio.

B. Anomalies detector

This test evaluates the pixels that show up as anomalies over the background. It is particularly indicated for point targets since changes on extended areas (i.e. distributed targets) will be rejected. In order to perform the test optimally, the pdf of target and clutter should be known, which requires a priori information that generally are not available for point targets. In this paper, only the pdf of the clutter is considered and a Constant False Alarm Ratio (CFAR) methodology is employed [20], which tries to keep constant the probability that one background pixel may be higher than the threshold (i.e. Probability of False Alarm P_f).

If ρ^M is the maximum between ρ_{12} or $\frac{1}{\rho_{21}}$ the test hypothesis are:

$$\begin{cases} H_0 = & \rho^M < T_s, \\ H_1 = & \rho^M \geq T_s, \end{cases} \tag{20}$$

and P_f can be calculated as:

$$P_f = 1 - \int_0^{T_s} f_R^{(n)}(r)dr. \tag{21}$$

The analytical solution of the integral is unknown and in our tests the integrations will be performed numerically. This makes the algorithm slower, but assures a solution with a desired level of accuracy.

The statistics of the background can be extracted locally following an ordinary methodology based on *guard* windows. The single pixel under analysis is surrounded by an area rejected by the analysis. Around the guard area, a ring of pixels is used to estimate the statistics of the clutter background. The windows dimensions depend on the sensor parameters (e.g. resolution) and the dimension of targets of interest. A graphical representation is provided in Figure 2.a, where the central red pixel is under test and the surrounding gray pixels are rejected by the analysis. Only the ring of brown pixels is used to extract the statistics of the background. More details on this will be provided in the validation section.

Few words should be spent regarding the estimation of the pdf parameters. The correlation ρ and ratio τ can be estimated in a straightforward way with a sample mean. The parameter more complicated to estimate is the Equivalent Number of Look, *n* which can be derived in a ordinary fashion considering the squared mean over the variance. The problem with such estimator is that it does not take into account eventual texture or generally some heterogeneity, that may bias strongly the resulting *n*. The strategy followed in this paper is to evaluate *n* locally over all the dataset (exploiting moving windows) and then select the value to use in a supervised way. More sophisticate ways can be devised that consider adaptive windows or segmentations. They are not treated in this paper since the main aim is to present the algorithms without altering too much the detection masks with supplemental pre- or post-

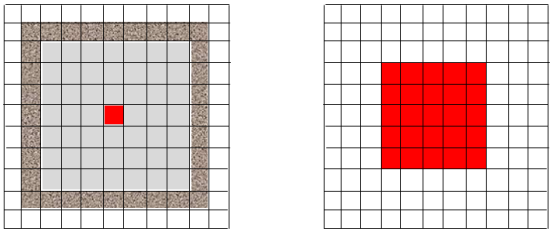

(a) Anomaly detector (b) Distributed Changes detector

Fig. 2. Examples of windows exploited by two statistical tests: (a) Guard moving windows for Anomaly Detector; (b) Simple box-car window for Distributed Changes detector.

processing. The latter may cover the real performances making not clear if the results are due to the proposed algorithms or to the pre- and post-processing.

C. Distributed Changes detector

In case that the detector is focused on distributed targets another statistical test is necessary, since the interest is focused on changes of the background itself (ring and central pixels belong to the same distribution). The test is based on selecting a *physical* threshold (T_p) and detecting the distributions of pixels that are above T_p with a sorter confidence (a probability of Detection P_d). T_p can be derived from models (physical or empirical) of target changes (e.g. due to different moisture content or different phenological stages of agricultural plants). Figure 2.b represent an example of window used in this test. Now, the only pixels employed in the analysis are the ones in the red region.

After setting T_p the P_d is calculated as:

$$P_d = 1 - \int_0^{T_p} f_R^{(n)}(r)dr. \tag{22}$$

Equivalently, the Probability of Missing Detection $P_m = 1 - P_d$ can be exploited. One detection is called when the probability that the distribution under analysis is above the threshold has a sorter value $P_d \geq \hat{P}_d$ (for instance 99.9%). From an intuitive point of view,

evaluating P_m means to test the left tail of the distribution, while evaluating P_f means to test the right tail.

D. Two stages test

In this last section the two previous statistical tests are combined to deal with point targets in changing clutter. As it will be showed in the validation section the anomaly detector suffers from a large false alarm rate. On the other hand, the Distributed Changes detector cannot be used for point targets in clutter because some distributed targets exhibiting changes may generate false alarms (this is when the focus is exclusively on point targets). For this reason, an initial anomaly detector is performed returning an initial threshold T_i. In order to avoid false alarms when the background is very stable an initial values for T_i is set. T_i is then used by a second Distributed Changes detector that evaluate the confidence that the distribution of pixels under analysis is above such threshold. This second stage will reduce more the false alarms since a collection of pixels is evaluated and not just one pixel.

In other words, the final algorithm is composed by two stages, the first estimate an initial threshold based on a probability of False Alarm estimated with a ring around a guard window and the second is based on a probability of detection estimated on an internal window (around the central pixel). Figure 3 shows a flow chart for the 2 Stages test.

IV. Validation with real data

A. Data Presentation

The algorithm is tested on two different quad-pol E-SAR data in L-band, both acquired in 2006. The first dataset is from the SARTOM campaign [22], and was specially focused on target detection with tomography and polarimetry. The resolution is $1.5\ m$ in slant range and

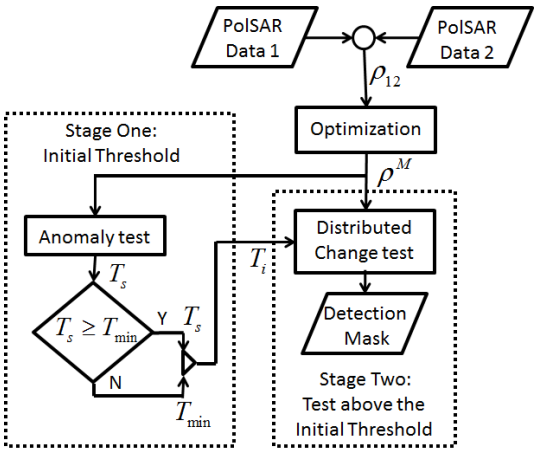

Fig. 3. Flow chart of the 2 Stages Detector. An initial threshold is evaluated during the first stage and then used by the second stage to set a test for a distributed target.

$0.9\ m$ in azimuth (the pixel sampling is $1.5\ m$ and $0.44\ m$ respectively). For this reason, in the test area, several targets were located in open field and under vegetation. Additionally, some of the targets were moved during the acquisitions. Figure 4 shows the RGB Pauli images of the test area for two separated acquisitions. The spatial baseline is zero (in average) and the temporal one is four days. Several targets among two trihedral corner reflectors (CR) in open field, one CR in the forest and two jeeps in open field were removed during the four days (they are indicated with red circles in the images). Details on the squares will be provided in the following.

The second dataset was acquired in the framework of the AGRISAR campaign [23]. Again, the resolution is $1.5\ m$ in slant range and $0.9\ m$ in azimuth (the pixel sampling is $1.5\ m$ and $0.44\ m$ respectively). The dataset is specially tailored for polarimetric observation of agricultural fields, therefore long time series of data are available. The two acquisitions exploited in this work were acquired the 5^{th} of July and the 2^{nd} of August (2006). RGB Pauli images are showed in Figure 5. Again, they have zero spatial baseline (in average) and the temporal one is about one month. Several fields appear to change significantly in the images.

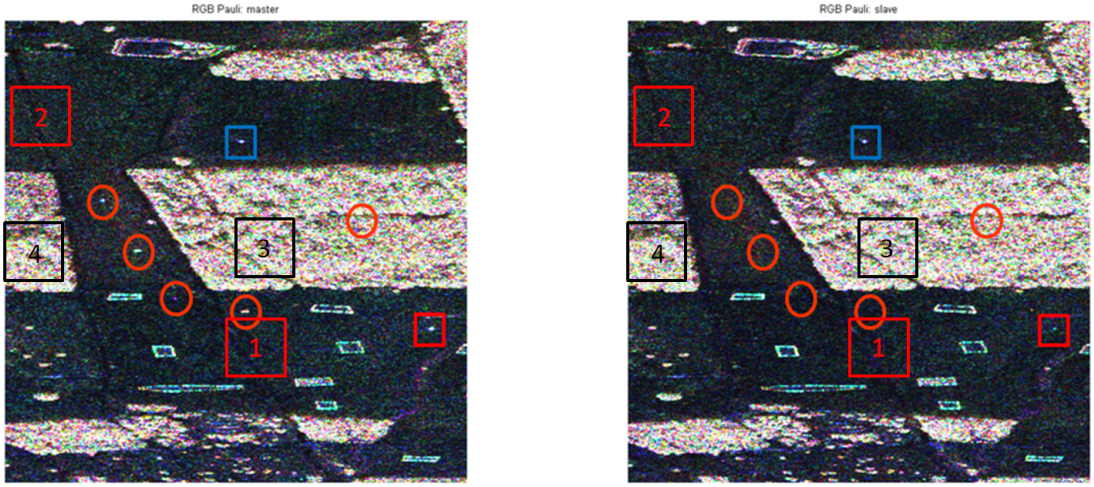

(a) Pauli RGB (master) (b) Pauli RGB (4 days after)

Fig. 4. RGB Pauli images of the SARTOM test site with 4 days of temporal baseline: (a) Master acquisition (b) Slave acquisition (4 days after). Red circles: targets removed; Red rectangle (without number): unknown target with visible change; Blue rectangle: target replaced after 4 days; Red rectangles (with number): bare ground with short grass; Black rectangles: coniferous forest approximately 20m high. Image size $1300x440\ m$ (DLR E-SAR L-band SARTOM2006 Campaign).

Moreover, the area covers some build up areas (the settlement of Göslow, close to Görmin, Germany). The area was selected because it shows two different fields, one harvested (without large changes) and another vegetated. The red and black squares indicate areas where a more detailed analysis will be carried out in the following.

Finally, Figure 6 presents two aerial photographs (taken from Google Earth) to compare with the SAR images. Please note, the distortion of the radar images is due to the non squared pixel.

B. Optimization of error factor

The first algorithm under analysis is the optimization of the error factor γ_e. The average used for the estimation of the power components exploited a 11x11 boxcar filter. The eigen-

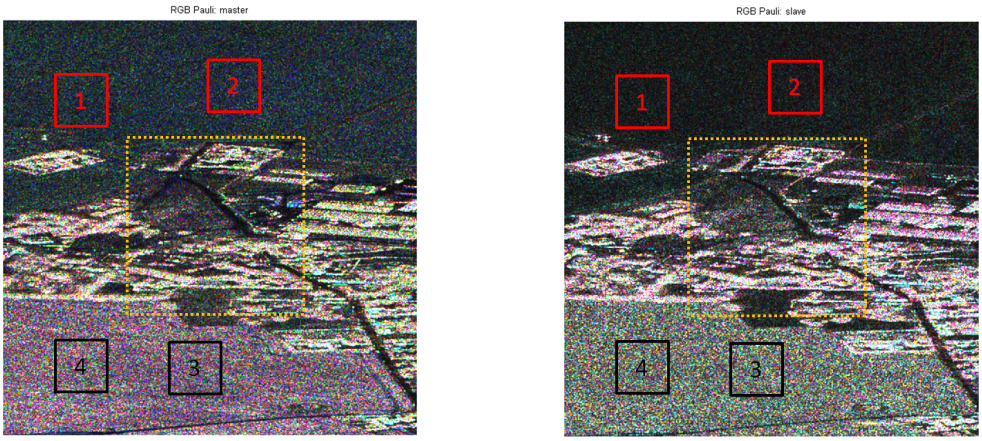

(a) Pauli RGB (master) (b) Pauli RGB (1 month after)

Fig. 5. RGB Pauli images of the AGRISAR test site: (a) Master acquisition; (b) Slave acquisition (1 month after). Red rectangles: winter wheat; Black rectangles: unknown crop; Orange rectangle: area used for further analysis. Image size $1300x440\ m$ (DLR E-SAR L-band AGRISAR2006 Campaign).

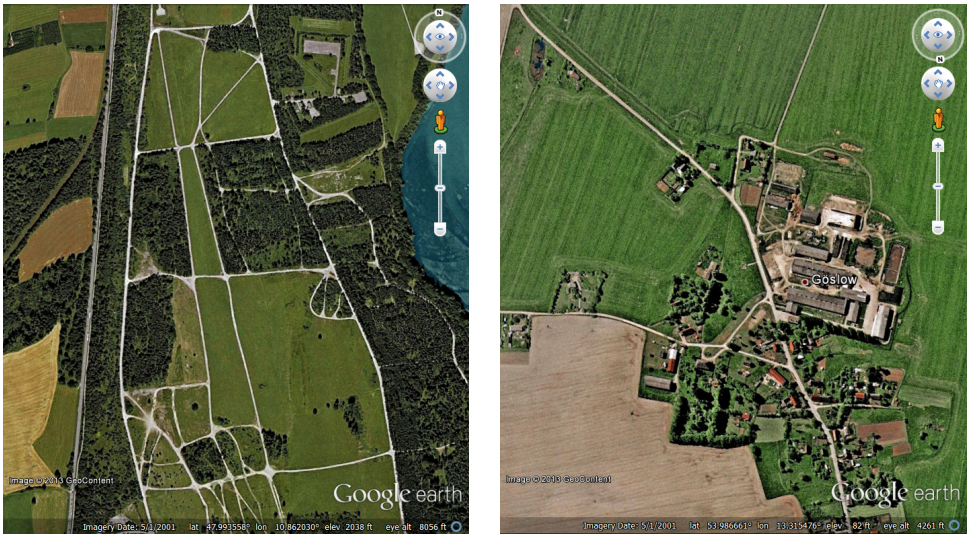

(a) SARTOM (b) AGRISAR 2006

Fig. 6. Google Earth aerial photographs of the two test sites: (a) SARTOM (b) AGRISAR 2006. Please note, the SAR images suffer a distortion due to the non squared pixel. Also, in the AGRISAR picture the North is pointing down.

values of the optimization over the SARTOM dataset are presented in Figure 7 (please note the scaling is different for the three images). The minimum of γ_e is particularly close to one (i.e. absence of error) except for few point targets. As a comparison the ratio for the second component of the Pauli decomposition is presented. $HH - VV$ was selected because it is sensitive to dihedral scattering which is generally strong for man-made targets. Forest and bare ground do not show significant changes after four days, nevertheless, it can be observed a slightly different temporal behavior where the ground changes more than the forest. During the two acquisitions the weather conditions were different with rain in the second acquisition. It could be speculated that the different moisture introduced more polarimetric difference on the ground compared to the forested areas. Please note, the movement of the scatterers and consequent interferometric temporal decorrelation do not translate generally in polarimetric changes. The maximum eigenvalue shows that seven point targets present a change larger compared with other areas. Five of these points are the known removed targets. In the next section, more details will be provided about the other two targets. A further remark should be made regarding the middle optimal point of γ_e. This is a stationary point (zero derivative), but it is not possible to predict if it corresponds to a maximum/minimum or a saddle point (the second derivatives should be evaluated). For this reason, it has to be considered with care.

The output of optimizing γ_e for the AGRISAR dataset is presented in Figure 8, with again the $HH-VV$ for comparison. At difference than the previous dataset, the distributed targets present large changes. This implies that the ESM hypothesis over such targets would lead to severe errors. Interestingly, the minimum eigenvalue can be relatively small also in areas where the partial target is changing significantly. This is a clear indicator that the change is mainly focused on a particular direction (i.e. single target) in the polarimetric space and

there are areas in the space where the change is not large. This leads to the idea that the eigenvectors may be used to try to understand the typology of change undertaken by the partial target. These are only speculations and more studies should be carried out to evaluate this possibility.

Finally, in order to check that the mathematical optimization is performed properly, ten points (five in the SARTOM and five in the AGRISAR dataset) were used to extract the coherency matrices $[T_{11}]$ and $[T_{22}]$. Then, a Monte Carlo simulation was used to generate one million random scattering mechanisms uniformly distributed on a unitary complex sphere on $\mathbb{C}^3$ and the quantity γ_e was evaluated using the coherency matrices. In all ten cases, the optimization was able to provide a maximum value of γ_e higher than the brute force algorithm even though in some cases these were very close each other.

C. Optimization of Power Ratio

The results of the optimization of ρ_{12} for the SARTOM dataset are presented in Figure 9. Again the coherency matrices were filtered with an 11x11 boxcar. As explained in previous sections, a large change may provide either a very large or very small ρ_{12} depending if the target is present in the first or second acquisition. The methodology followed here is to invert the eigenvalue when this is smaller than one and change its sign (i.e. making it negative). The resulting variable was defined as $\hat{\rho}_{12}$. To ease the visual interpretation, a rainbow colortable can be used, where red is for changes where the first acquisition is higher and blue where the second acquisition is higher. Such visualization is showed in Figure 10 for the maximum and minimum eigenvalues. A complementary way to show the optimization results could be to produce an image with the highest values of eigenvalues and inverted eigenvalues for each pixel (i.e. to have one single image with the maximum change possible). This representation

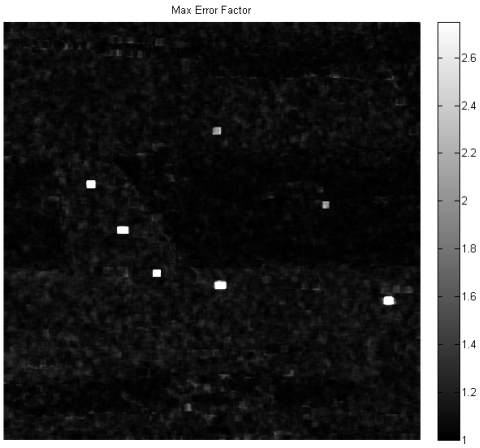

(a) Maximum γ_e

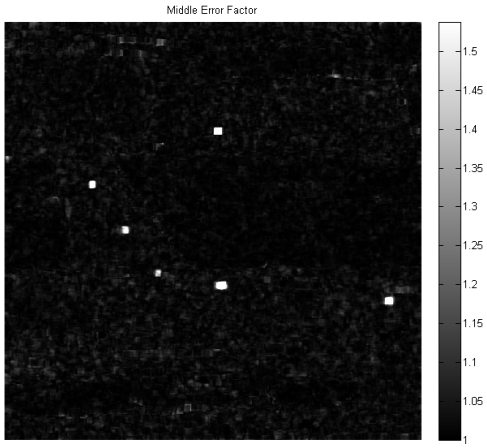

(b) Middle γ_e

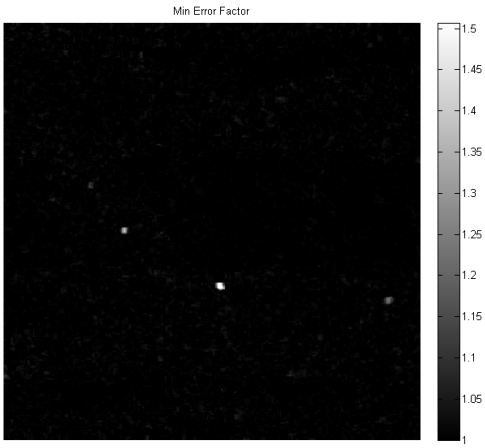

(c) Minimum γ_e

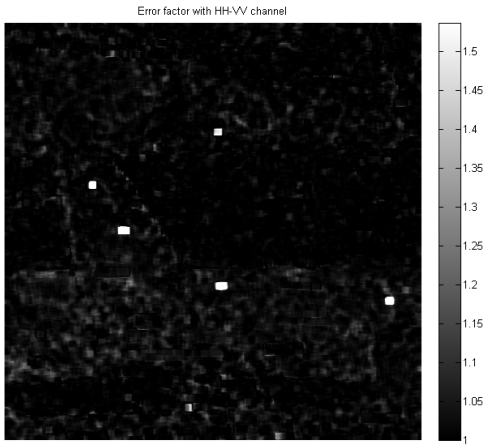

(d) HH-VV

Fig. 7. Optimization of the error factor γ_e (SARTOM). (a) Maximum γ_e; (b) Middle γ_e; (c) Minimum γ_e; (d) Error factor for $HH - VV$. Averaging: 11x11 boxcar.

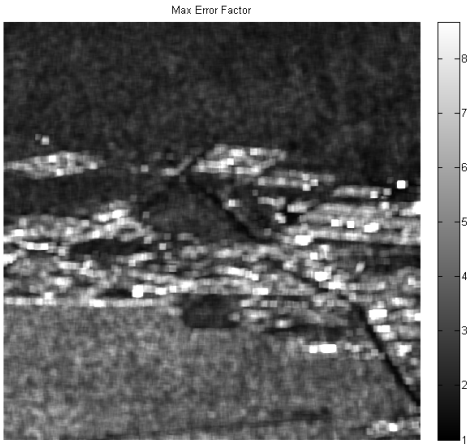

(a) Maximum γ_e

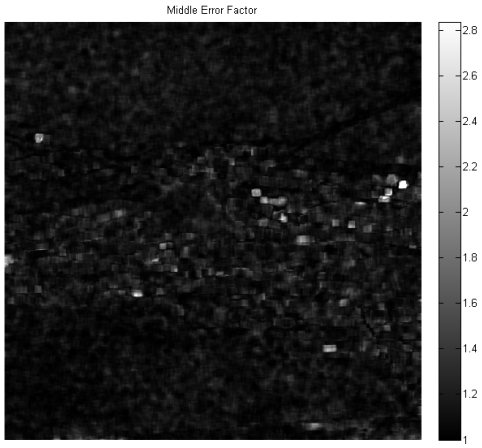

(b) Middle γ_e

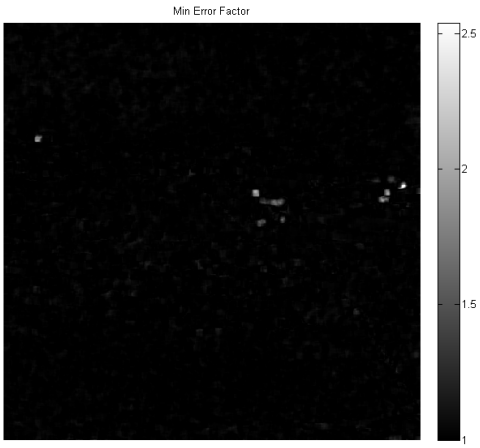

(c) Minimum γ_e

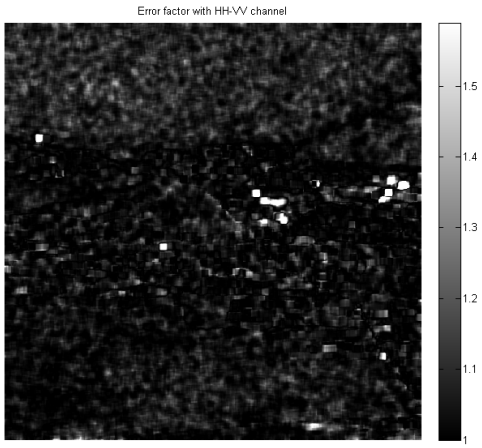

(d) HH-VV

Fig. 8. Optimization of the error factor γ_e (AGRISAR). (a) Maximum γ_e; (b) Middle γ_e; (c) Minimum γ_e; (d) Error factor for $HH - VV$. Averaging: 11x11 boxcar.

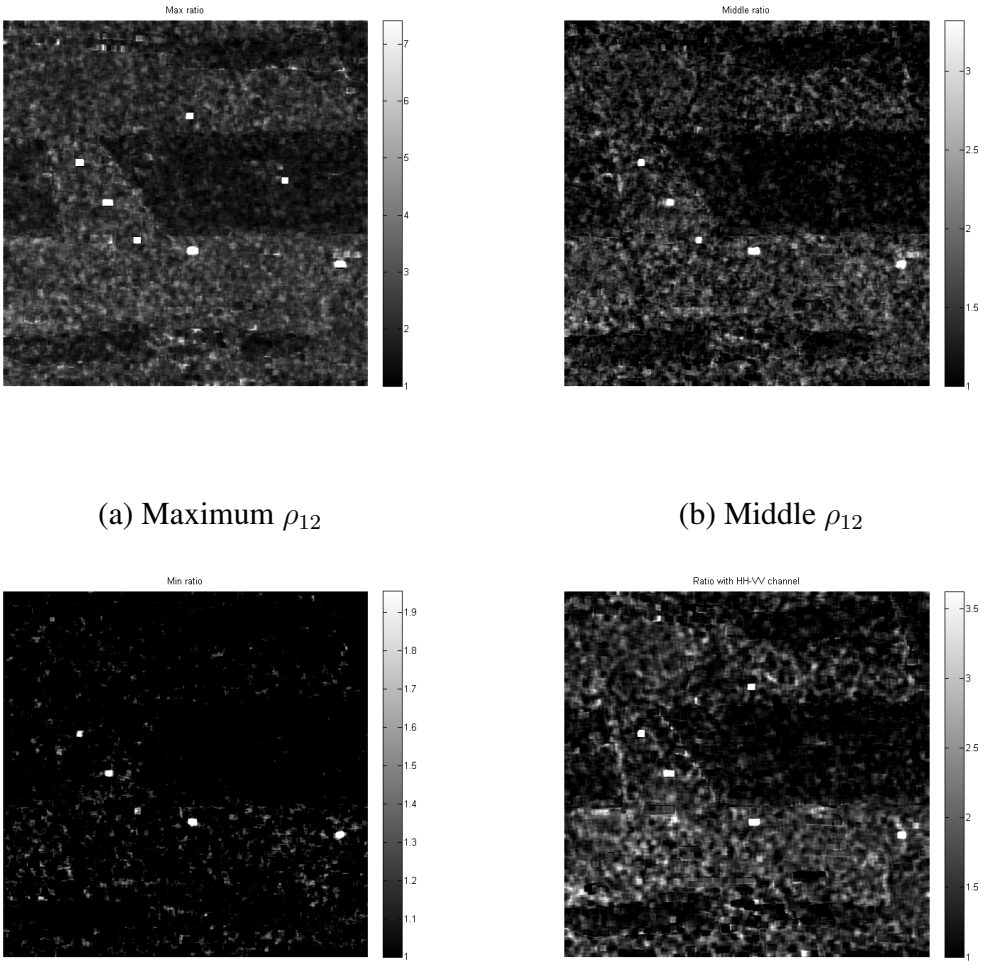

(a) Maximum ρ_{12} (b) Middle ρ_{12}

(c) Minimum ρ_{12} (d) Ratio with HH-VV

Fig. 9. Power ratio optimization (SARTOM): (a) Maximum of ρ_{12} (b) Middle of ρ_{12}; (c) Minimum of ρ_{12}; (d) Ratio evaluated with $HH - VV$. Averaging: 11x11 boxcar.

is avoided here because it will mix the results of the different eigenvalues masking the real output of the algorithm.

All the targets with validated changes can be easily detected with the maximum eigenvalue, including the corner reflector under canopy cover. Interesting, using only the $HH - VV$ the latter cannot be detected anymore. Two further point targets have a relatively large ratio. The one in the red rectangle seems to almost disappear in the second acquisition as a

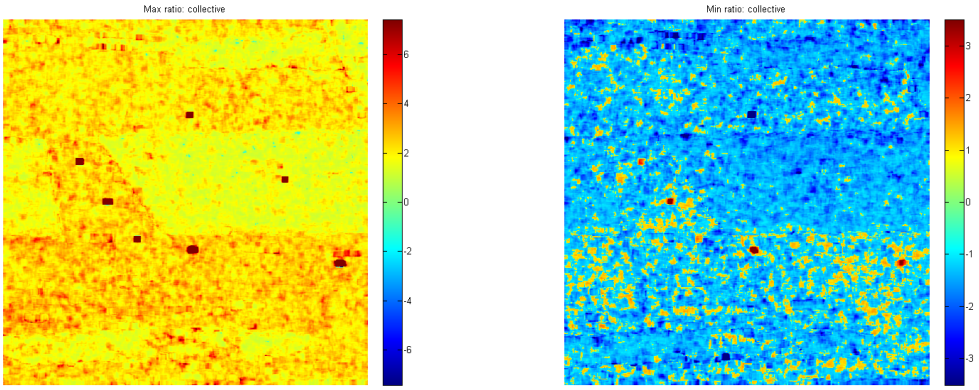

(a) Maximum $\hat{\rho}_{12}$ (b) Minimum $\hat{\rho}_{12}$

Fig. 10. Power ratio optimization after modifying the ratio (SARTOM): (a) Maximum of $\hat{\rho}$ (b) Minimum of $\hat{\rho}$. The red is for changes where the target is present in the first acquisition and blue for targets present in the second acquisition. Averaging: 11x11 boxcar.

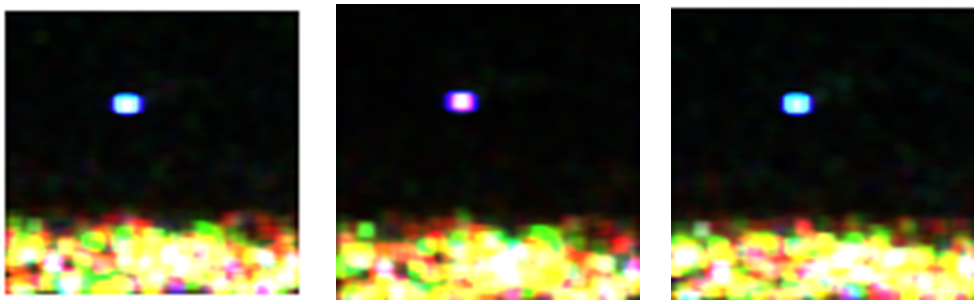

(a) Master (b) Slave (4 days after) (c) Slave (after 40min)

Fig. 11. Pauli RGB images of a corner reflector (SARTOM): (a) Master acquisition; (b) Slave acquisition, 4 days after the Master (the one exploited in the previous analysis); (c) Slave acquisition, 40min after the Master (it is not used in the rest of the manuscript). The corner reflector was removed and relocated on the forth day (it was not used for calibration purposes).

portion of it was removed. Unfortunately, a ground survey for this target is not available to confirm this speculation. The point in the blue rectangle is a trihedral corner reflector positioned on the ground without pedestal. This was removed at the end of the first acquisition and then replaced on the ground four days after. It was not used for calibration purposes, but it only functioned as a target to detect. In order do have some insight on this corner reflector another acquisition is considered, taken 40min after the Master (during this 40 minutes the corner reflector was not touched). A zoom of the Pauli RGB images is provided in Figure 11 and reveals that the color around the corner reflector appears different in the two acquisitions. The reason for such difference in backscattering and polarimetric behavior is unknown to the authors, nevertheless, the visible change can be detected by the algorithm.

Figure 12 shows the results of the ρ_{12} optimization on the AGRISAR dataset. Here only the rainbow masks are presented for sake of brevity. As already observed, the field at the bottom of the image is suffering the largest changes as well as the buildup areas. Interestingly, the minimum eigenvalue shows that there are some targets present in the second acquisition but not in the first one. Using the $HH - VV$ error is not possible to evaluate that the bottom field is suffering larger changes than the up one (even though these are clearly evident also in the RGB image).

It is interesting to notice that the optimization is able to pick up more changes in the farm building than the ratio of HH-VV. To check that this changes are really present in the data, a brief polarimetric analysis is performed on a smaller area (for an easier visualization) which is zoomed on some farm buildings. Figure 13 presents the entropy and mean alpha angle as derived by the Cloude-Pottier decomposition (i.e. eigenvector problem of the Coherency matrix) [7]. The red rectangles in the α images help identifying some areas where α (which is linked to the scattering mechanism) changes. Some of these areas appear in the maximum

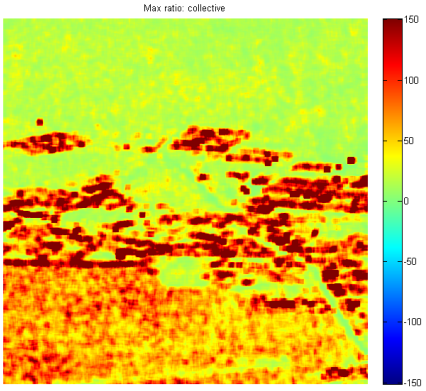

(a) Maximum $\hat{\rho}_{12}$

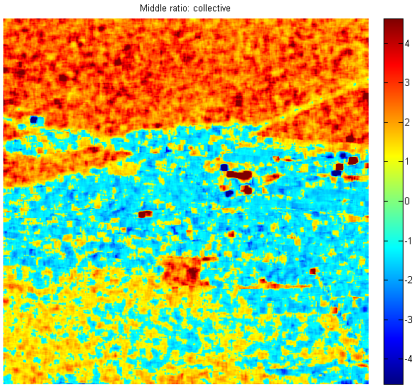

(b) Middle $\hat{\rho}_{12}$

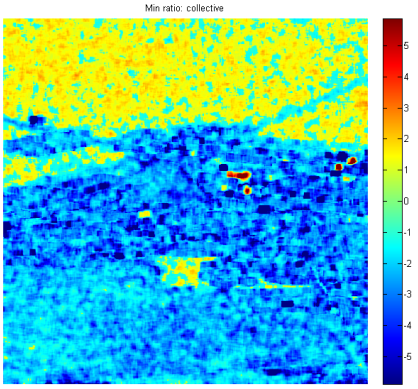

(c) Minimum $\hat{\rho}_{12}$

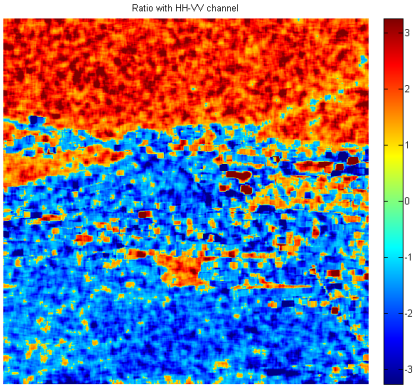

(d) Ratio for HH-VV

Fig. 12. Power ratio optimization (AGRISAR): (a) Maximum of $\hat{\rho}$ (b) Middle of $\hat{\rho}$; (c) Minimum of $\hat{\rho}$; (d) Ratio for $HH - VV$. The red is for changes where the target is present in the first scene and blue for targets present in the second scene. Averaging: 11x11 boxcar.

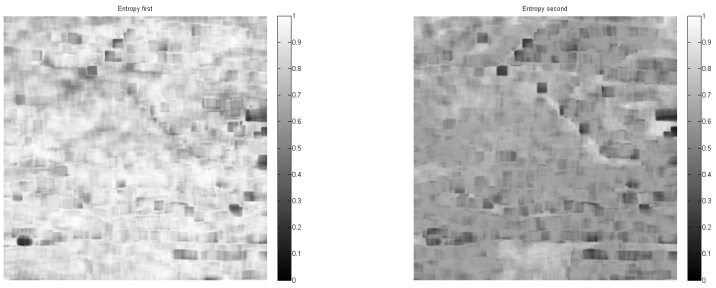

(a) Entropy first (b) Entropy second

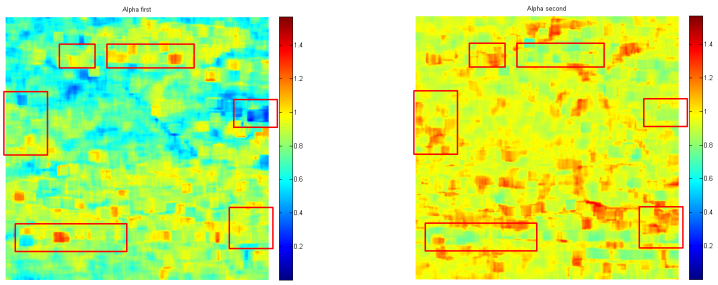

(c) Averaged α first (d) Averaged α second

Fig. 13. Cloude-Pottier decomposition of the Coherency matrices: (a) Entropy of first acquisition; (b) Entropy of second acquisition; (c) Averaged α of first acquisition; (d) Averaged α of second acquisition. The red rectangles identify some of the changes in the entropy that can be identified with the maximum eigenvalue of the optimization, but not with the single channel ratio. Averaging: 11x11 boxcar.

eigenvalue of the power ratio, but they can not be identified in the ratio of $HH - VV$.

As for the γ_e, a Monte Carlo simulation was employed to perform a brute force maximization of ρ_{12} and again the Lagrange methodology provides the highest value.

V. Statistical tests

In this section, a test of fit for the theoretical pdf and an analysis of the statistical tests are provided. Again, the SARTOM and AGRISAR dataset will be employed to highlight the different behavior of the tests for point and distributed targets.

A. Test of IR pdf

A test of fit for the intensity ratio pdf for two polarimetric channels (e.g. co-polarizations ratio) was already performed in [10], here the focus is on the output of the optimization of ρ_{12}. Theoretically, the pdf should still fit the data as long as the area under analysis is homogeneous (which is also one fundamental hypothesis for the derivation of the IR pdf). To test these, the two E-SAR dataset are exploited.

Firstly, four areas in the SARTOM dataset were selected (both red and black rectangles in Figure 4), two of them are bare ground (with short grass) and other two are forested areas (coniferous approximately 20m high). Each of the areas is a tile of 80x80 pixels. The histograms of the maximum ratio and the theoretical pdf are presented in Figure 14. In comparing histograms and theoretical pdf, care was given in exploiting identical horizontal axis and normalizing both over their integral. In order to have a more exhaustive analysis the Cumulative Distribution Function CDF is presented in Figure 15.

A simple visual interpretation of the curves seems to suggest that the fit may be adequate even though it is not perfect. The CDF allow a deeper look at the tails of the distributions which are of large interest for detection purposes. Specifically, it seems that Ground1 and Forest4 show the largest difference in the CDF. This is visible in the pdf with a higher peak of the histogram resulting in a sharper increase of the CDF. Such difference may also be related to imprecision in estimating the pdf parameters (as explained previously).

In general, the visual interpretation may have some limitations, therefore in this paper some Goodness-of-Fit (GoF) tests were exploited in order to have a more quantitative analysis [24]. In this context a very large variety of GoF tests could be exploited and a thorough comparison goes outside the purpose of this paper. Here, only two very well-known

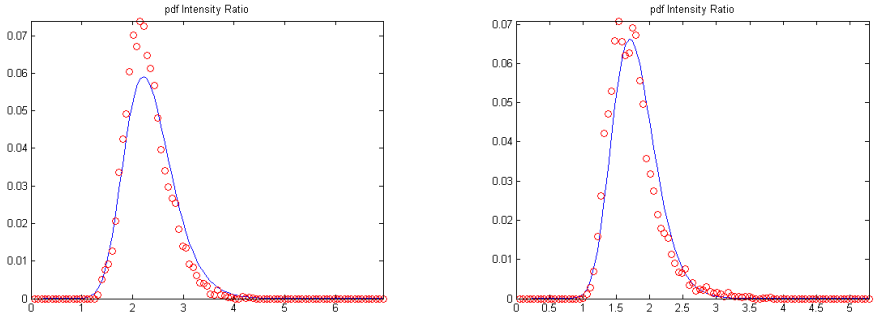

(a) Ground1 (b) Ground2

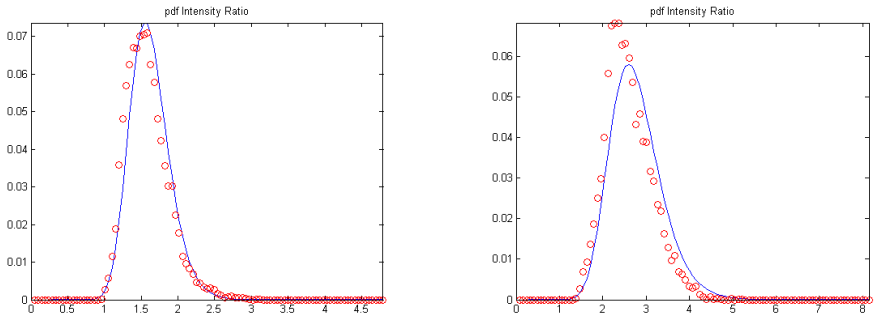

(c) Forest3 (d) Forest4

Fig. 14. pdf of optimized ρ_{12} for the SARTOM data. Red circles: histogram points (data); Blue line: fitted pdf.

tests are considered (one focused on the pdf and the other on the CDF). The first test is the Kolmogorov-Smirnov (KS) two samples test:

$$D_{ks} = \max_x \|F_1(x) - F_2(x)\|, \tag{23}$$

where F_1 and F_2 are the CDF of the two random variables under analysis. Knowing the distributions it is possible to set a threshold on D_{ks} with a sorter confidence value: $P(D_{ks} > D_n) = \alpha$. This means that the CDF of the data will be contained in the theoretical CDF with a probability of $1 - \alpha$. Here, such final probability is set to 95%

The second test is the Pearson's Chi-Squared (χ^2) test. The test statistics is:

$$X^2 = \sum_i \frac{(f_o(i) - f_e(i))^2}{f_e(i)}, \tag{24}$$

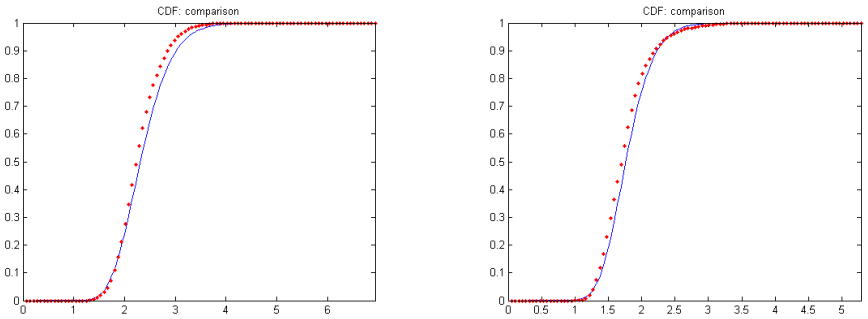

(a) Ground1 (b) Ground2

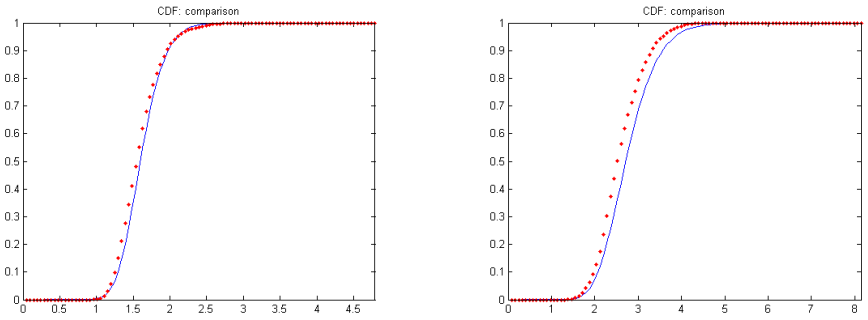

(c) Forest3 (d) Forest4

Fig. 15. CDF of optimized ρ_{12} for the SARTOM data. Red circles: histogram points (data); Blue line: fitted CDF.

where f_o is the observed pdf (the histogram) and f_e is the expected (theoretical) pdf. Such test statistics X^2 should be a χ^2 distribution with a defined degree of freedom. The distribution of X^2 is tested and the hypothesis that observed and theoretical distributions are the same is rejected if X^2 is not χ^2. A confidence value can again be set using a parameter α in order to associate a probability to the fit. In this paper, the value of α was set to 0.05, as for the previous case.

All the areas passed both the tests showing that the fit should have a confidence of at least 95%. The observed suitability of the IR pdf encouraged the exploitation of such distribution for the automatic detectors. Clearly, the use of local estimators (as showed in the following tests) would not be able to estimate properly the pdf parameters in case the area is not

homogeneous. In the latter situation, some pre-segmentation scheme may improve the performance. Another factor that is important to take into account is the number of samples used to compare the theoretical and observed distributions. In this paper, 80x80 pixels were used to estimate the fitting parameters, but then of this 100 random samples were exploited by the GoF test (since this is approximately the number of pixels used by the adaptive detector). A value N can be calculated as:

$$N = \frac{N_1\ N_2}{N_1 + N_2}, \tag{25}$$

where N_1 is the number of samples from the theoretical pdf and N_2 from the data. In our case, $N_1 = N_2$, therefore $N = N_1/2 = 50$. As a rule of thumb, in order to have an adequate test the value of N should be greater or equal than four (i.e. eight samples each).

The pdf of the intensity ratio was derived under the assumption of complex Gaussian pixels, however, SAR intensity images in some cases present texture (i.e. a fluctuation of the radar cross-section). Therefore, it is important to understand if the pdf for the ratio can still be used when some moderate texture is present in the data. A widely used model for texture on intensity images is the K-distribution [21]. The description of such distribution is outside the purpose of this paper, here it is only mentioned that one of the pdf parameters is called *order parameter* ν and is a good indicator for the presence of radar cross-section fluctuations (i.e. texture). In particular, for $\nu \to \infty$ the cross section is constant and the K-distribution reduces to a Gamma distribution (where the Gaussian hypothesis is fulfilled), while for $\nu \to 0$ the texture effects are very evident. The estimation of ν is not very easy since the Maximum Likelihood Estimator does not have a closed form. For this reason, some different estimators (which require numerical solution), has to be employed. In this paper, the "Normalized Logarithm of Intensities" is used since it showed good results as long as the

Number of independent Looks is large enough [21], [25]. The estimator can be written as:

$$\ln \langle I \rangle - \langle \ln I \rangle = \ln \nu - \Psi^0(\nu) + \ln L - \Psi^0(L), \tag{26}$$

where I is the averaged intensity, Ψ^0 is the digamma function and L is the Equivalent Number of Looks. The value of ν was derived solving the expression in numeric. The area of analysis contained 80x80 pixels and the intensity pixels were averaged with a 11x11 boxcar filter.

The resulting values of ν for the areas are reported in the following: $\nu\{Ground1\} = 1.3$; $\nu\{Ground2\} = 0.92$; $\nu\{Forest3\} = 0.5$; $\nu\{Forest4\} = 0.9$. The estimated values of ν show the presence of some texture that may be also seen in the intensity images (e.g. clearings in forests and paths on bare ground). From these results, it may be inferred that the IR pdf does not appear particularly sensitive to texture, since the histograms still fit the theoretical pdf. A possible explanation is that if the radar cross section fluctuations are equal in the two acquisitions (i.e. the change behavior is preserved by the different texture components) then the texture will cancel out in the ratio.

The second experiment considers the AGRISAR data. The changes here are much higher and it is interesting to understand if the IR statistical model is still valid when the mean ratio is largely higher than one. The large rectangles in Figure 5, shows the areas used for estimating the distributions. Two areas are on a harvested field (i.e. bare ground) presenting a relatively low backscattering and low changes (presumably due to growing of short grass). The second two areas are in a vegetated field presenting large backscattering which is changing due to different phenological stages (i.e. the periodic plant and animal life cycle events). The pdf and CDF of the areas with fitted theoretical distributions are showed respectively in Figure 16 and 17.

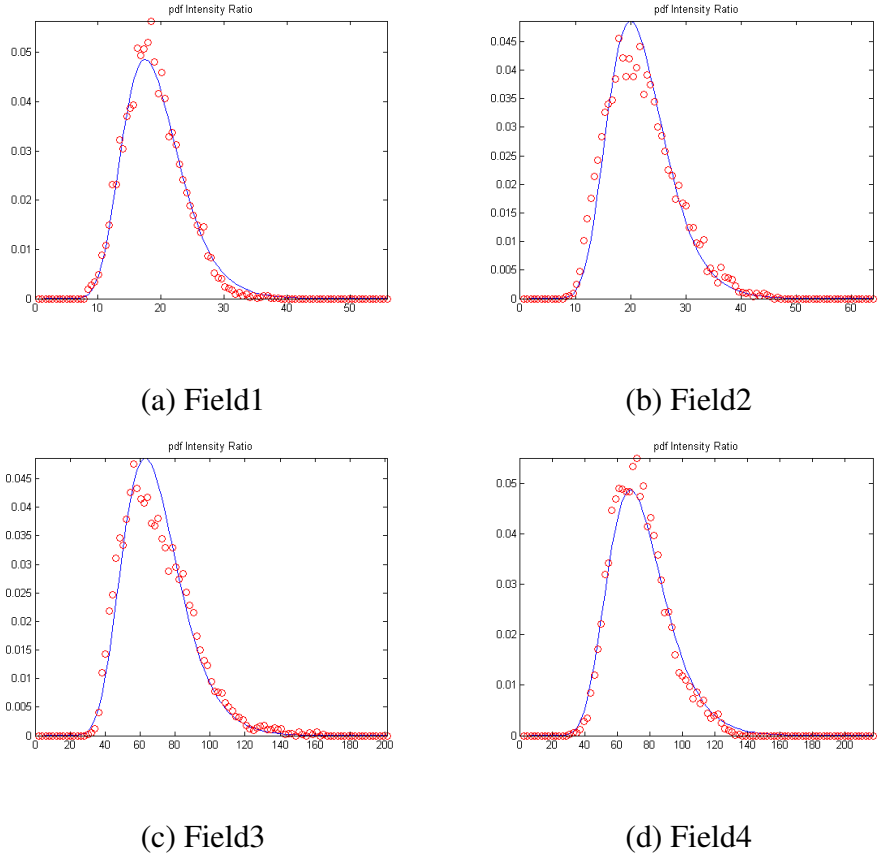

(a) Field1 (b) Field2

(c) Field3 (d) Field4

Fig. 16. pdf of optimized ρ_{12} for the AGRISAR data. Red circles: histogram points (data); Blue line: fitted pdf.

Again the fit appears adequate even though Field1 and Field3 show some differences on the maximum value of the peak (as exhibited previously). Again the KS and the χ^2 tests are performed in order to check that the fit has some statistical significance. All the areas passed the KS and the χ^2 tests with $N = 50$. The estimation of the order parameter ν was repeated for this second dataset as well. The resulting values of ν for the fields are reported in the following: $\nu\{Field1\} = 1.96$; $\nu\{Field2\} = 1.24$; $\nu\{Field3\} = 2.48$; $\nu\{Forest4\} = 2.66$. In this dataset the texture effects are less strong and this is also visually evident from the intensity images, where the fields appears more homogeneous.

As a final summary, the KS and χ^2 test showed that it should be possible to use the IR distribution as a general model, however, some problem may be encountered in case of areas

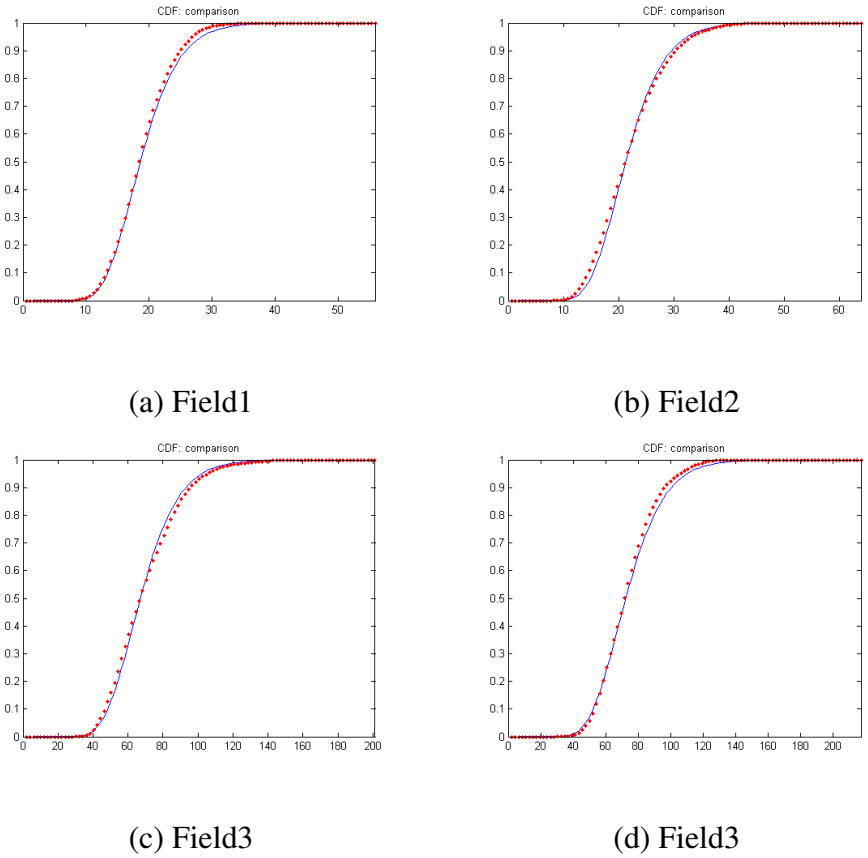

(a) Field1 (b) Field2

(c) Field3 (d) Field3

Fig. 17. CDF of optimized ρ_{12} for the AGRISAR data. Red circles: histogram points (data); Blue line: fitted CDF.

that show large texture effects especially if the different targets do not present an homogeneous behavior in time (i.e. they change in different way). Possible future work in this direction could consider a pre-segmentation step.

B. Anomaly detector

This test is especially suited for point targets. In this experiment, the guard window is a squared 21x21 pixels, while the clutter window is a ring one pixel broad around the guard window (i.e. 88 pixels in total). Two probabilities of False Alarms are exploited: $P_f = 10^{-6}$ and $P_f = 10^{-8}$.

The resulting detection masks over the SARTOM dataset are presented in Figure 18, where

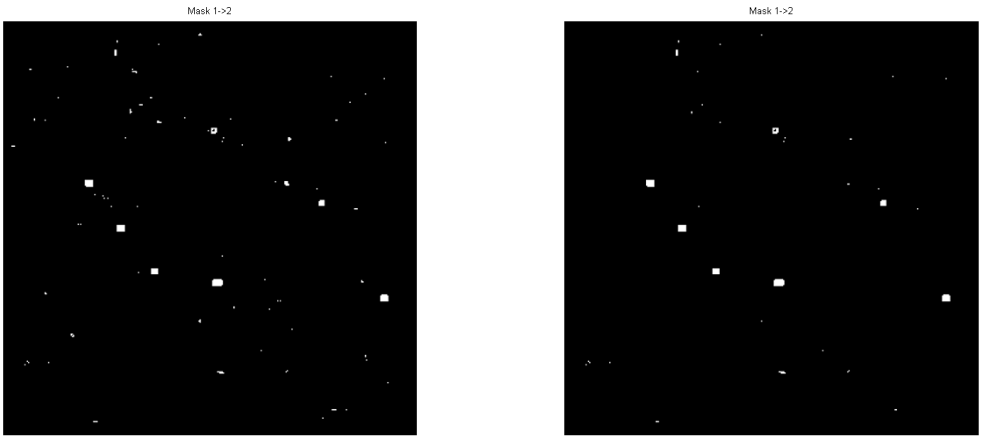

(a) $P_f = 10^{-6}$ (b) $P_f = 10^{-8}$

Fig. 18. Anomaly detection for $\max(\rho_{12})$ (SARTOM). (a) $P_f = 10^{-6}$; (b) $P_f = 10^{-8}$.

many false alarms are evident. Even though, modifying the P_f or estimating more accurately the pdf parameters the number of false alarms should reduce, the authors believe that their occurrence has a more profound reason and is intrinsic of the anomaly test. When the background is particularly stable in the two images (i.e. its correlation ρ is proximal to one) the standard deviation of the ratio is very small (proximal to zero) and the threshold will be set near the mean value (which is proximal to one). In these circumstances, the likeliness that a small change in the central pixel is above the threshold is rather high. From a statistical point of view, those detected points are not false alarms, however, they do not correspond to genuine real-targets and they should be rejected. As for most detectors, the final mask may always be improved and cleaned adding some post-processing algorithms (e.g. a morphological opening filter), but this will not solve the methodological issues. To conclude, the authors suggest care in evaluating the mask of the anomaly detector and different tests are proposed in the following.

For the sake of completeness, the same anomaly test is performed on the AGRISAR data and showed in Figure 19, again with probabilities $P_f = 10^{-6}$ and $P_f = 10^{-8}$. The detections

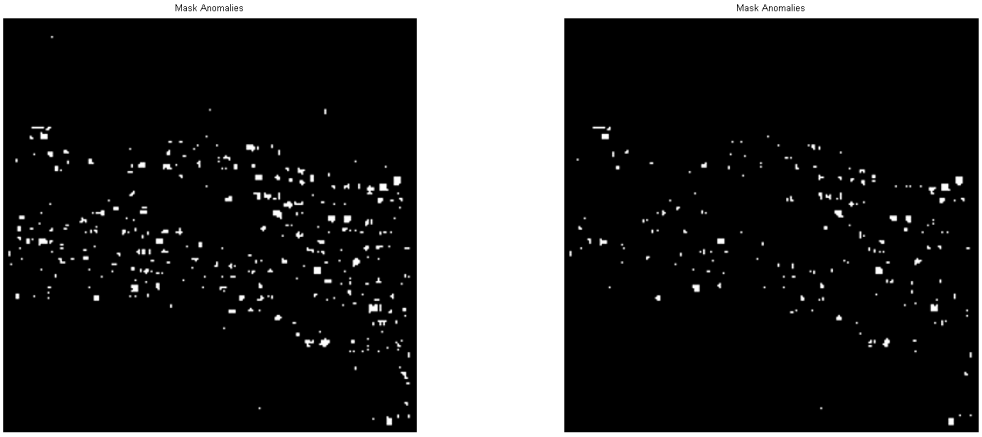

(a) $P_f = 10^{-6}$ (b) $P_f = 10^{-8}$

Fig. 19. Anomaly detection for $\max(\rho_{12})$ (AGRISAR). (a) $P_f = 10^{-6}$; (b) $P_f = 10^{-8}$.

are mainly located in the buildup areas and should correspond to point targets (e.g. vehicles that were moved or just parked with a different orientation with respect to the flight path).

C. Distributed Changes detection

The test is mainly focused on distributed targets and selects areas that are above a defined threshold with a P_d higher than a sorter value (the P_m can be equivalently used). In this particular experiment, the area considered to estimate the pdf contains 11x11 pixels. The probability of missing detection is chosen as $P_m = 0.001$.

The results for the SARTOM dataset are showed in Figure 21, with thresholds equal to $T_p = 2$, $T_p = 5$, $T_p = 10$ and $T_p = 20$.

The false alarms are reduced strongly except when the value of T_p is particularly low. With a threshold $T_p = 5$ it is possible to detect all the targets that changed in the scene (including the corner reflector that was only slightly moved). With the threshold equal to 10 or 20 only large changes are detected.

The AGRISAR dataset is probably more adequate for this kind of detection, since this

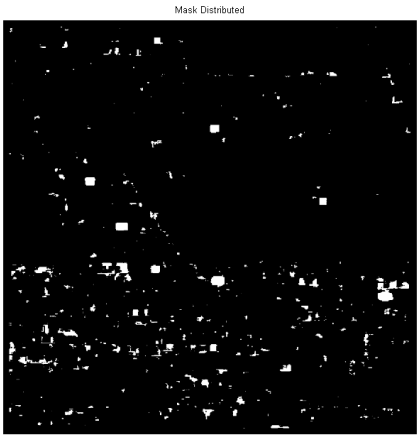

(a) $T_p = 2$

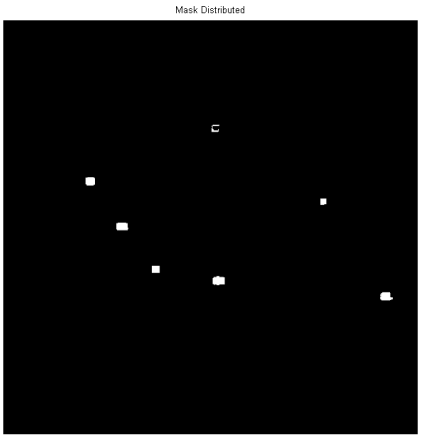

(b) $T_p = 5$

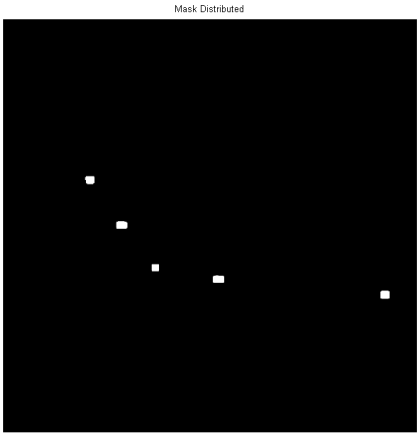

(c) $T_p = 10$

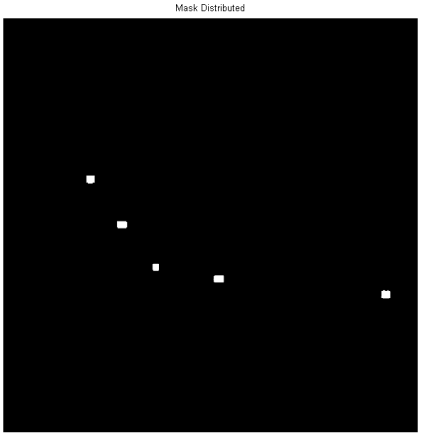

(d) $T_p = 20$

Fig. 20. Distributed Changes detection over SARTOM data for $\max(\rho_{12})$. $P_m < 10^{-3}$. (a) $T_p = 2$; (b) $T_p = 5$; (c) $T_p = 10$; (d) $T_p = 20$.

test site presents an abundance of dynamic distributed targets. Considerable larger changes are expected on agricultural fields, different values of the physical threshold are selected: $T_p = 10$, $T_p = 20$, $T_p = 50$ and $T_p = 100$. Interestingly, it can be observed that the two main fields (up and bottom of the image) can be separated based on the amount of changes. In particular, the uppermost field does not change more than $T_p = 20$. Moreover, the bottom field would not be detected with $T_p = 50$ or $T_p = 100$. The buildup area again presents the highest changes among the observed land covers.

D. Two stage test

The final test tries to combine the previous two in order to produce an automatic algorithm for detection of point targets in dynamic clutter. The P_f of the first stage anomaly detector is 10^{-6}, the second test is performed with $P_m = 0.001$ and the minimum value for the anomaly threshold is $T_i = 5$, since this was showed a robust value in the previous tests.

The resulting detection mask for the SARTOM and AGRISAR dataset are presented in Figure 22. All the targets that experienced a change in the SARTOM dataset are detected, included the corner reflector inside the forest and the one that was moved. In the AGRISAR data the detector is able to pick up the differences in the built up area neglecting the fields. Unfortunately, a validation for the vehicles location in the AGRISAR settlements is not available.

As a final remark, it has to be said that in order to compare more appropriately different algorithms (also including other typologies of detectors) more data accompanied by ground measurements should be acquired. With such dataset, valuable tools to compare different detectors such as Receiver Operating Characteristics (ROC) curves can be estimated. Unfortunately, ROC curves could not be assessed exploiting the current datasets for two main

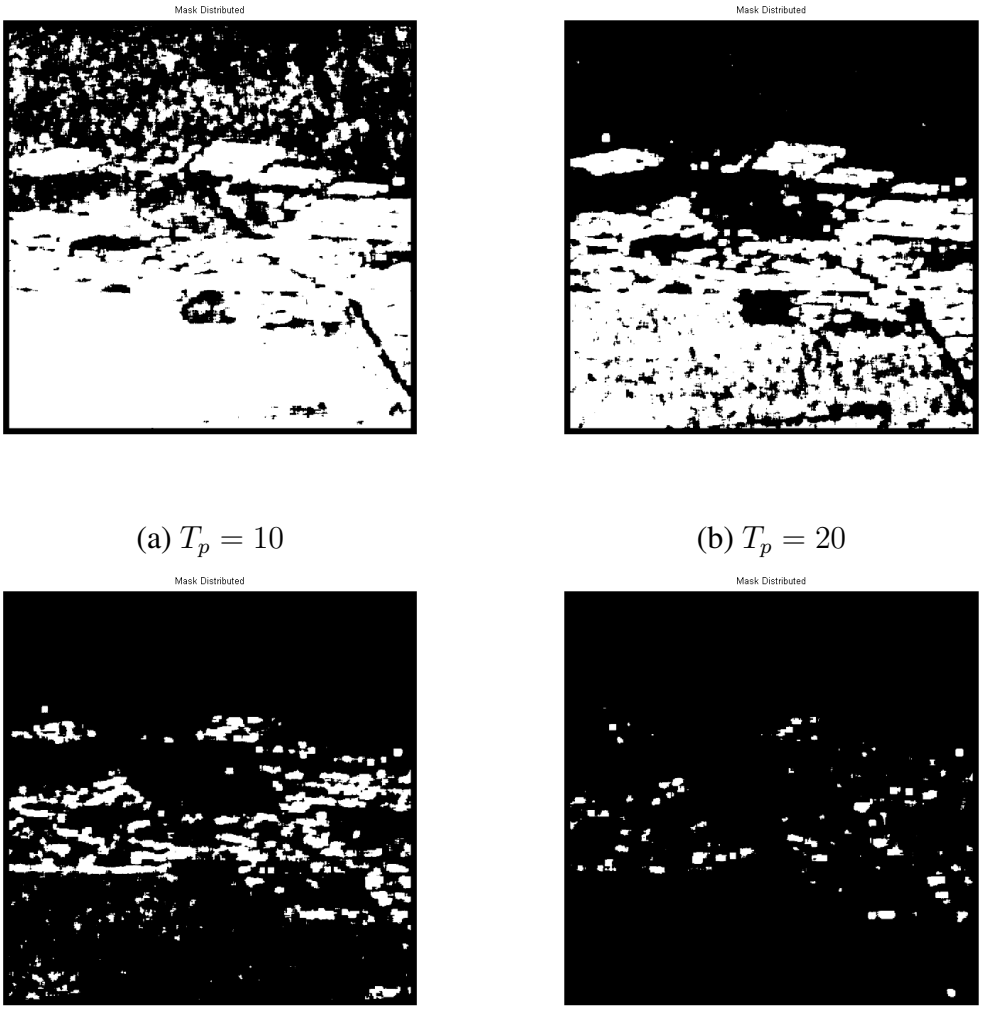

(a) $T_p = 10$ (b) $T_p = 20$

(c) $T_p = 50$ (d) $T_p = 100$

Fig. 21. Distributed Changes detection over AGRISAR data for $\max(\rho_{12})$. $P_m < 10^{-3}$. (a) $T_p = 10$; (b) $T_p = 20$; (c) $T_p = 50$; (d) $T_p = 100$.

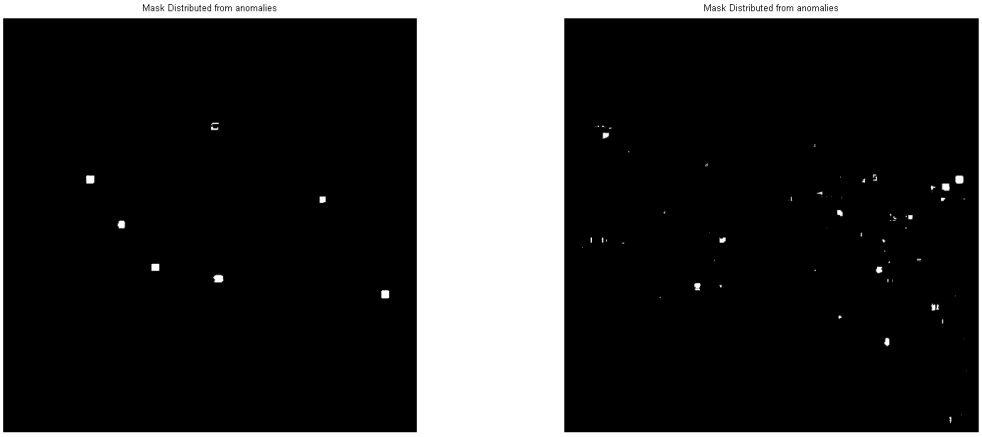

(a) SARTOM (b) AGRISAR

Fig. 22. Combined detector for (a) SARTOM and (b) AGRISAR dataset. $P_f = 10^{-6}$, $P_m = 0.001$, minimum $T_i = 5$.

reasons. Firstly, only five targets in the entire scene have validated changes and this cannot provide an accurate estimation of the probability of detection. Secondly, ancillary information regarding the rest of the scene is not available, hence it is not trivial to find an extensive unchanged area to estimate the false alarm rate (i.e. many detections that could be classified as false alarms may actually be genuine changes). For this reason, a more extensive analysis and validation exploiting ROC curves is left as future work.

CONCLUSIONS

In this work, two analytical optimizations exploiting a Lagrange methodology are proposed. The first is aimed at an error factor γ_e for the Pol-InSAR coherence when an Equi-Scattering Mechanism hypothesis is performed, while the second is focused on an intensity ratio ρ_{12} varying the scattering mechanism. Both the optimizations can be accomplished with eigen-problems. Interestingly, it was demonstrated that the eigenvectors resulting from the two diagonalizations are the same. The detectors are finalized with thresholds on the

respective eigenvalues.

In the second part of the paper, three statistical tests are devised for the power ratio ρ_{12}. The tests are based on the pdf of the Intensity Ratio (IR) proposed by Lee *et al.* [10], which assumes that the SLC complex pixel can be modeled as complex Gaussian random variable. The first test is an anomaly detector evaluating differences between the background clutter and a central pixel under analysis. This algorithm is adaptive, using guard windows to extract the clutter statistics and it is more appropriate for detecting changes to point targets. The second test analyzes an area of interest detecting the pixel distributions that are above a physical threshold with a sorter confidence. The threshold can be set a-priori knowing the typology of target to be observed. This test is more appropriate for distributed targets. Finally, one last test combines the first two in a two stage algorithm, in order to devise a detector for point targets embedded in dynamic clutter.

The algorithms were tested on two different quad-polarimetric L-band E-SAR DLR dataset. The first was acquired during the SARTOM 2006 campaign and it is largely dedicated to point target detection, while the second is from the AGRISAR 2006 campaign and is focused on agricultural observation (i.e. changes suffered by distributed targets). Both dataset are accompanied by ancillary ground data. Some of the vehicles/targets in the SARTOM dataset were removed in between the two acquisitions and the AGRISAR agricultural fields were experiencing known changes. The optimization results were adherent to the ground information and visual interpretation. The theoretical pdf was tested over several areas in the two dataset showing adequate visual fitting. Moreover, all the areas passed the Kolmogorov-Smirnov and the χ^2 test with 95% confidence except one field in the AGRISAR dataset that did not pass the χ^2 test. The distribution for such field appeared to be multi-modal with areas inside the field that were experiencing very little change. In this context, a pre-segmentation

stage may improve the fit.

The statistical tests for the power ratio were examined on the two dataset. It was observed that the anomaly detector suffers from large false alarm rate. This is because the test detects very small anomalies when the background is particularly stable (for this reason the authors suggest caution when using it). The second test is more beneficial for detecting changes of distributed targets (as the fields in the AGRISAR dataset). Additionally, it was possible to discriminate between different land covers based on the magnitude of their change. Finally, the two stage test showed good results either on the SARTOM or the AGRISAR dataset. In the latter, it was possible to isolate the point targets and reject the large agricultural fields. As a final recommendation, the choice of the statistical test depends on the focus of the detection. If distributed targets are of interest (e.g. changing in backscattering due to soil moisture) the Distributed Changes detector should be used, on the other hand if the focus is on point targets (e.g. vehicles) than the 2-Stage detector should be exploited.

APPENDIX

E. γ_e and ρ_{12} have the same eigenvectors

A well-known theorem that will be exploited in the following is the sequent: giving two diagonalizable matrices $[Q]$ and $[Q]^p$, they have the same eigenvectors and eigenvalues $\lambda_{[Q]} = \lambda^p_{[Q]^p}$ [18]. Consequently, $[T_{22}]^{-1}[T_{11}]$ and $[T_{11}]^{-1}[T_{22}]$ has the same eigenvectors and inverse eigenvalues. The two matrices to test are $[A_1] = \frac{1}{4}\left([T_{22}]^{-1}[T_{11}] + 2[I] + [T_{11}]^{-1}[T_{22}]\right) = [U_1][\Sigma_1][U_1]^{*T}$ and $[A_2] = [T_{22}]^{-1}[T_{11}] = [U_2][\Sigma_2][U_2]^{*T}$, where $[U_1]$ and $[U_2]$ are two unitary matrices where the columns are the eigenvectors. It is possible to write, $[\Sigma_1] = [U_1]^{*T}[A_1][U_1]$ and $[\Sigma_2] = [U_2]^{*T}[A_2][U_2]$. Substituting the matrices $[A_1]$ and $[A_2]$ it can be

derived:

$$\begin{aligned}[\Sigma_1] =& \frac{1}{4}\left([U_1]^{*T}[T_{22}]^{-1}[T_{11}][U_1]\right.\\ &\left.+ 2[U_1]^{*T}[I][U_1] + [U_1]^{*T}[T_{11}]^{-1}[T_{22}][U_1]\right)\\ =& \frac{1}{4}\left([U_1]^{*T}[T_{22}]^{-1}[T_{11}][U_1] + 2[I]\right.\\ &\left.+ [U_1]^{*T}[T_{11}]^{-1}[T_{22}][U_1]\right)\\ [\Sigma_2] =& [U_2]^{*T}[T_{22}]^{-1}[T_{11}][U_2]. \end{aligned} \tag{27}$$

By definition $[U_2]$ diagonalize $[T_{22}]^{-1}[T_{11}]$, therefore, it will also diagonalize $[T_{11}]^{-1}[T_{22}]$. Since $[I]$ is already diagonal, if $[U_1]$ is set equal to $[U_2]$, $[\Sigma_1]$ will be the sum of diagonal matrices and therefore still diagonal. Because the diagonalization is a unique operation, $[U_2]$ or a permutation of $[U_2]$ (i.e. rearrangement of columns) must be the only possible unitary matrix $[U_1]$ that diagonalize $[\Sigma_1]$. For this reason, $[U_1] = [U_2][P]$, with $[P]$ any permutation matrix. To summarize, the eigenvectors are the same even though their ranking (linked to the value of the eigenvalues) may be different.

F. The eigenvalues for γ_e and ρ_{12} are real positive

The eigenvalues resulting the optimization of γ_e and ρ_{12} are generally different, however they both keep the property of being real positive. In order to demonstrate this, the product of matrices $[T_{11}]^{-1}[T_{22}]$ can be considered. They are both Hermitian semi-positive definite matrices (the inverse of a Hermitian matrix is still Hermitian). For convenience, it is written $[T_{11}]^{-1} = [B]$ and $[T_{22}] = [C]$, with $[B]$ and $[C]$ any Hermitian semi-positive definite matrices. We want to demonstrate that $[B][C]$ has real positive eigenvalues. Please note, this does not mean that $[B][C]$ is semi-positive definite (i.e. $\underline{\omega}^{*T}[B][C]\underline{\omega} \notin \mathbb{R}^+$) unless $[B]$ and $[C]$ are commuting matrices (i.e. $[A][B] = [B][A]$). If the diagonalization of each matrix is

performed it is possible to write:

$$[B] = [U_B][\Sigma_B][U_B]^{*T}, \tag{28}$$
$$[C] = [U_C][\Sigma_C][U_C]^{*T}.$$

where $[U_B]$, $[U_C]$ are unitary matrices and $[\Sigma_B]$, $[\Sigma_C]$ are diagonal matrices. The product $[B][C]$ can be written as:

$$[B][C] = [U_B][\Sigma_B][U_B]^{*T}[U_C][\Sigma_C][U_C]^{*T}. \tag{29}$$

It can be demonstrated that similarity transformations do not change the eigenvalues of a matrix (which are basis invariant). The selected similarity is $[U_B][\Sigma_B]^{-\frac{1}{2}}[U_B]^{*T}$. Therefore, after the similarity is applied we have:

$$[U_B][\Sigma_B]^{\frac{1}{2}}[U_B]^{*T}[U_C][\Sigma_C][U_C]^{*T}[U_B]^{*T}[\Sigma_B]^{\frac{1}{2}}[U_B]. \tag{30}$$

Considering, $[U_B][\Sigma_B]^{\frac{1}{2}}[U_B]^{*T} = [B]^{\frac{1}{2}} = [D]$ is Hermitian, it can be written: $[D][C][D]^{*T}$. The latter is Hermitian since, $[D][C][D]^{*T} = \left([D][C][D]^{*T}\right)^{*T}$ and therefore it is diagonalizable and have real positive eigenvalues. Considering $[D][C][D]^{*T}$ has the same eigenvalues of $[B][C]$, then the latter is diagonalizable and has real positive eigenvalues.

Once proved that $[T_{11}]^{-1}[T_{22}]$ has real positive eigenvalues, it is straightforward to extend this to the matrix $\frac{1}{4}\left[[T_{22}]^{-1}[T_{11}] + 2[I] + [T_{11}]^{-1}[T_{22}]\right]$, since it can be decomposed in the sum of three components each one with real positive eigenvalues and equal eigenvectors.

ACKNOWLEDGMENTS

The SARTOM2006 and AGRISAR2006 data were acquired by the E-SAR airborne system of DLR. The SARTOM data were provided by DLR, while the AGRISAR2006 data were provide by ESA. The authors would like to thank the DLR team that participated to the

SARTOM campaign in 2006, in particular Ralf Horn, Matteo Nannini and Rolf Scheiber. A final thank goes to Simon Zwieback (ETH Zürich) for the interesting discussions about the fascinating World of non Hermitian matrices and their relevance in modern society.

REFERENCES

[1] M. Preiss and N. J. S. Stacy, *Coherent Change Detection: Theoretical Description and Experimental Results*, Defence Science and Technology Organisation, 2006.

[2] E. J. M. Rignot and J. J. Van Zyl, "Change detection techniques for ERS-1 SAR data," *IEEE Transactions on Geoscience and Remote Sensing*, vol. 31(3), pp. 896–906, 1993.

[3] R. Dekker, "SAR change detection techniques and applications," *25th EARSeL Symposium Global Developments in Environmental Earth Observation from Space Porto, Portugal*, 2005.

[4] R. J. Radke, S. Andra, O. Al-Kofahi, and B. Roysam, "Image change detection algorithms: a systematic survey," *IEEE Transactions on Signal Processing*, vol. 14(3), pp. 294 – 307, 2005.

[5] J. F. Mas, "Monitoring land-cover changes: A comparison of change detection techniques," *International Journal of Remote Sensing*, vol. 20(1), pp. 139–152, 1999.

[6] L. M. Novak, "Coherent change detection for multi-polarization SAR," *Conference Record of the Thirty-Ninth Asilomar Conference on Signals, Systems and Computers, 2005.*, pp. 568 – 573, 2004.

[7] S. R. Cloude, *Polarisation: Applications in Remote Sensing*, Oxford University Press, 2009.

[8] S. R. Cloude and K. P. Papathanassiou, "Polarimetric SAR interferometry," *IEEE Transactions on Geoscience and Remote Sensing.*, vol. 36(5), pp. 1551–1565, 1998.

[9] K. P. Papathanassiou and S. R. Cloude, "Single-baseline polarimetric SAR interferometry," *IEEE Transactions of Gesciences and Remote Sensing*, vol. 39(11), pp. 2352–2363, 2001.

[10] J. S. Lee and E. Pottier, *Polarimetric radar imaging: From basics to applications*, CRC Press, Taylor & Francis Group, 2009.

[11] K. Conradsen, A. A. Nielsen, J. Schou, and H. Skriver, "A test statistic in the complex Wishart distribution and its application to change detection in polarimetric SAR data," *IEEE Transactions on Geoscience and Remote Sensing*, vol. 41(1), 2003.

[12] S.R. Cloude and K.P. Papathanassiou, "Three-stage inversion process for polarimetric SAR interferometry," *IEE Proceedings Radar, Sonar and Navigation*, vol. 150(3), pp. 125,134, 2003.

[13] M. Neumann, L. Ferro-Famil, and A. Reigber, "Multibaseline polarimetric SAR interferometry coherence optimization," *IEEE Geoscience and Remote Sensing Letters*, vol. 5(1), 2008.

[14] A. Marino, *A New Target Detector Based on Geometrical Perturbation Filters for Polarimetric Synthetic Aperture Radar (POL-SAR)*, Springer-Verlag, 2012.

[15] A. Marino, S. Cloude, and I. H. Woodhouse, "Detecting depolarizing targets using a new geometrical perturbation filter," *IEEE Transactions on Geosciance and Remote Sensing*, vol. 50(10), pp. 3787–3799, 2012.

[16] A. Marino, S. R. Cloude, and J. M. Lopez-Sanchez, "A new polarimetric change detector in radar imagery," *IEEE Transactions on Gescience and Remote Sensing*, vol. 51(5), pp. 2986 – 3000, 2013.

[17] S. Boyd and L. Vandenberghe, *Convex Optimization*, Cambridge, Cambridge University Press, 2004.

[18] G. Strang, *Linear Algebra and its Applications*, Thomson Learning, 1988.

[19] L.M. Novak, M.B. Sechtin, and M.J. Cardullo, "Studies of target detection algorithms that use polarimetric radar data," *IEEE Transactions on Aerospace and Electronic Systems*, vol. 25(2), pp. 150–165, 1989.

[20] S. M. Kay, *Fundamentals of Statistical Signal Processing*, Prentice Hall, 1993.

[21] C. Oliver and S. Quegan, *Understanding Synthetic Aperture Radar Images.*, SciTech Publishing, Inc, 2004.

[22] R. Horn, M. Nannini, and M. Keller, "SARTOM airborne campaign 2006: Data acquisition report.," *DLR-HR-SARTOM-TR-001*, 2006.

[23] Microwaves German Aerospace Center and Radar Institute (HR), *AGRISAR 2006 Agricultural Bio-/Geophysical Retrievals from Frequent Repeat SAR and Optical Imaging*, Final Report: European Space Agency, 2008.

[24] E. L. Lehmann and J. P. Romano, *Testing Statistical Hypotheses*, Springer, 2005.

[25] N. J. Redding, *Estimating the Parameters of the K-Distribution in the Intensity Domain*, DSTO Electronics and Surveillance Research Laboratory, 1999.